ISSN 0915-633X

NATIONAL INSTITUTE FOR FUSION SCIENCE

Changes of the Electron Density Distribution during MHD Activity in CHS

H. Soltwisch, K. Tanaka

(Received - Aug. 8, 2000)

NIFS-643 Sep. 2000

RESEARCH REPORT
NIFS Series

TOKI, JAPAN

Changes of the electron density distribution during MHD activity in CHS

H. Soltwisch*, K. Tanaka**

* *Ruhr-University Bochum, Institute for Experimantal Physics, D-44780 Bochum, Germany*

** *National Institute for Fusion Science,322-6,Oroshi,Toki, 509-5292,Japan*

Abstract

Density oscillations induced by MHD activities were observed in NBI heated plasmas on CHS by using an HCN laser interferometer. The accompanied changes of the density profiles were also observed. The oscillations are composition of m=0 sawteeth like crash and m=2 sinusoidal oscillations as a post courser of the crash. Possible models of the oscillation structure are examined in order to explain experimental data of the interferometer. Rotating plasma core, which is hollow profile and keeps constant elongation of the flux surface can explain amplitude and phase distribution of the sinusoidal oscillation.

Keywords: CHS, HCN laser interferometer, MHD activity, sawteeth , MHD burst

1. Introduction

In the Compact Helical System (CHS) heliotron/torsatron it has been observed that repetitive MHD burst phenomena occur under certain discharge conditions. In previous investigations[1] a heavy ion beam probe has been used to study periodic changes in the electrostatic potential profile and to correlate these changes with magnetic field fluctuations as they were detected by an array of Mirnov coils. Concomitant oscillations of the electron density distribution have been noticed, but a detailed analysis of the relevant data, which were provided by a far-infrared interferometer, has been hindered so far by instrumental limitations and by the intricacy to convert line-integrated measurements into local information. It is the aim of the present work to address these problems and to complement the existing data base on MHD burst phenomena in CHS by additional information about the behaviour of the electron density profile.

In order to improve the spatial resolution of the three-channel interferometer, a series of very similar discharges was made, and one of the (horizontal) probing beams was shifted from shot to shot in vertical direction. In this way, twelve lines of sight in the lower half of the plasma cross-section became available, although with irregular spacing due to access limitations. To account for shot-by-shot variations, the signals were normalised, and the data were combined so as to represent a set of interferometric phase shift signals for one typical discharge.

In this typical discharge the temporal evolution of the density profile was investigated by using a generalized Abel inversion technique. For this purpose, the non-circular magnetic surfaces in CHS were approximated in analytical form by a set of nested contour lines, and it was assumed that the density was constant on a given flux surface. Owing to the fact that only horizontal lines of observation were available, it was impossible to distinguish unambiguously between deformations of the magnetic surfaces (i.e. deviations from the vacuum magnetic field structure) and local changes of the electron density. Nevertheless, in order to gain some insight into the global (or macroscopic) evolution, the analysis was performed under the assumption that the shape of the magnetic flux surfaces remained constant throughout the discharge. Since this supposition is obviously not justified during strong MHD activity, the experimental data were averaged in time to "smooth out" periodic oscillations. As a result, only perturbations with poloidal mode number $m = 0$ could be detected.

A more detailed investigation of higher-order perturbations was impeded not only by the limited number of probing beams and their parallel orientation but also by a rather poor reproducibility of fast signal oscillations in subsequent discharges. However, since only one of the three interferometric beams was moved from shot to shot, the two fixed channels could be used to synchronize the burst events in different shots and to establish amplitude and phase relations among the signals measured at different positions. From these it became clear that the MHD activity introduced a fairly strong $m = 2$ perturbation of the density profile. Attempts were made to localize this mode and to determine its spatial extent by performing model calculations for a variety of different shapes and sizes and by comparing the results with the experimental data. It was found, however, that the available signals are still too sparse for obtaining an unambiguous picture of the density perturbation during MHD burst phenomena in CHS.

2. Evaluation of the Global Density Profile

This section describes the techniques and procedures by which the experimental data of the laser interferometer are combined to form a consistent data set for a "typical" discharge, and by which this set of data is analysed with respect to global (or macroscopic) changes of the electron density profile. Since the magnetic field structure is assumed to be fixed (corresponding to the vacuum field distribution) and since the measured signals are averaged in time to suppress fast oscillations, the results represent only those changes which correspond to a $m = 0$ mode pattern. Fine structures due to higher-order modes will be discussed in section 3.

2.1. Preparation of the experimental data

The far-infrared interferometer operates at a wavelength of $\lambda = 0.337$ mm and comprises three horizontal probing beams[2]. Two of these beams are in a fixed position, while the third one can be moved in vertical direction. The locations of the beams in the non-circular cross-section of CHS are shown in Fig. 1.

The free electrons in the plasma cause in each probing wave a phase shift $\Delta\varphi$ which is given by

$$\Delta\varphi = r_e \lambda \int_{L(z)} n_e \, ds \qquad (1)$$

where $r_e = 2.818 \times 10^{-15}$ m denotes the classical electron radius, n_e is the electron density, and ds is the path element of the beam. The quantities $\Delta\varphi$ are measured by digital phase counter[2,3]. A 620kHz intermediate frequency (IF) signal for heterodyne detection was digitized at 100kHz and the effective IF signal frequency was 20kHz. Then, phase shift $\Delta\varphi$ was numerically calculated by using digital phase demodulation techniques. The calculated phase have a limited range from −180° to +180° and cause phase jumps at overflow, which have to be eliminated prior to further data processing (a suitable FORTRAN routine may be found in Appendix 5.1). Figure 2 shows an example of typical time traces obtained from the interferometer after correction of phase jumps.

2.1.1. noise reduction

As can be seen in Fig. 2, all traces return to their base line after the plasma pulse, which indicates a fairly high mechanical stability of the interferometric set-up. However, the signals are infested by considerable noise. The spectral composition has been determined in the time interval from 0 to 10 ms (that is, before plasma ignition) by means of a FFT routine, and the results are shown in Fig. 3. Obviously, by filtering out a spectral band between 12 and 17 kHz, the purity of the signals can be much improved (black lines in Fig. 3).

The fast signal oscillations caused by MHD activity during the burst phenomena have frequencies of a few kHz. Therefore the noise reduction will not significantly impair the plasma-induced features. Since, at this stage of the data analysis, we are only interested in the "average" behaviour of the density profile, we apply a low-pass filter with a cut-off frequency of 500 Hz or, alternatively, form a sliding average over 120 data points (corresponding to a time interval of 1.2 ms; both procedures result in fairly smooth and very similar signal traces).

2.1.2. combination of different shots

The discharges selected for analysis are listed in the following table together with the respective position of the movable probing beam and the average phase shift $\overline{\Delta\varphi_{center}}$ in the central beam for the time interval from 80 to 120 ms (the latter is formed by calculating the mean value of the data points number 8000 to 12000 of the raw signals after correction for phase jumps). The quantity $\overline{\Delta\varphi_{center}}$ serves to adjust all signals to a common level and thereby account for shot-by-shot variations (the normalisation factors are also given in the table).

In Fig. 4 the phase shift signals (after filtering and normalisation) are superimposed. The central channel yields nearly identical signal traces (with the exception of shot #72210, where the lower beam is close to the plasma edge at a position of −13.6 cm and is, therefore, of minor importance). By contrast, the fixed beam in the upper half of the plasma cross-section exhibits some scatter which points to a slight irreproducibility of the shape of the electron density profile in the selected series of discharges. For our purposes we will use the data of the moved channel (lower subfigure) and regard them as being measured in a single representative shot.

2.2. *Abel inversion in non-circular geometry*

Having available a set of phase shift data, which covers one half of the plasma cross-section, and assuming that the local electron density is constant on (given) magnetic surfaces, the density profile in CHS can be found in the following way (see Fig. 5 for illustration):

By using a set of closely spaced surfaces, the plasma cross-section may be divided into a number of annular zones, on which n_e is approximately constant. Hence, the path of a probing beam intersecting these zones is split up into small segments, and the line integral for the phase shift (equation (1) on page 2) may be expressed as a finite sum of these segments. A beam traversing just the outermost zone is represented by a single term only, which provides immediately the local density at the plasma edge. This information is then used to calculate the edge contribution to the signal of the adjacent beam passing through the next inner zone, which leaves us after subtraction with the local density in the second ring. Continuing this procedure, we can gradually advance towards the centre.

In practice, the number of actual measurements at different beam positions z is rather small and has to be replenished by a reasonable interpolation. For this purpose we will use a spline fit as described in section 2.2.2. Moreover, for the ease of calculation it is desirable to have an analytical formula for the shape of the contour lines.

2.2.1. analytical description of flux surfaces

As a starting point, we use the results of a numerical computation of the flux surfaces in CHS under vacuum conditions. A closer inspection of these contours reveals that they are well approximated by two semi-ellipses with a common minor axis as shown in Fig. 6 (only the outermost surfaces are not so well reproduced, but here the density – and hence the contribution to the total phase shift – will be small). Having in mind the inversion procedure outlined before, we are mainly interested in the distance L which the probing beam covers inside a surface. It is easy to prove that this distance depends only on the sum $(b_1 + b_2)$ of the major axes of the semi-ellipses but not on their ratio b_1/b_2. So, for our purposes it is sufficient to characterise each surface by two numbers: the height $2a$ (where a is the common minor axis of the ellipses), and the length $2b = (b_1 + b_2)$. Taking the given data of the numerical computation for the vacuum field structure, we plot b as a function of a (Fig. 7) and find that the dependence may be expressed as

$$b = (b_1 + b_2)/2 \cong 1.02 \cdot a \cdot \exp(0.036 \cdot a) \quad (2)$$

Hence, the distance L, which a probing beam at vertical position z covers inside a flux surface of height a, can be written as

$$L(z,a) \cong 2.04 \cdot \sqrt{a^2 - z^2} \cdot \exp(0.036 \cdot a) \quad (3)$$

2.2.2. construction of the phase shift profile

As has been mentioned before, the experimental data (i.e. the actual measurements taken at different beam positions) are rather sparse. For inverting the phase shift data and calculating a reasonable density distribution it is necessary to construct a complete phase shift profile $\Delta\varphi(z)$ with well-defined boundary conditions (the first derivative of $\Delta\varphi(z)$ has to be zero at $z = 0$ and at the plasma boundary $z = a_{\max}$; otherwise the resulting n_e-profile would exhibit a non-zero slope in the centre and an unphysically steep gradient at the edge). To satisfy these conditions and to provide a sensible completion of the few experimental points, a cubic spline interpolation with prescribed slopes at the end points can be used.

As an example, Fig. 8 shows the phase shifts versus probing beam position measured in our "typical" discharge during the time interval from 110 to 115 ms (cf. Fig. 4; the experimental data have been averaged to suppress signal oscillations caused by MHD activity). Because of access limitations at CHS, the data points are mainly concentrated between z = 5.3 cm and z = 9.3 cm, and outside this range the spline fit has to bridge rather large gaps. On the other hand, the closely spaced points introduce some structure to the phase shift profile. So, the function $\Delta\varphi(z)$ is a combination of "smooth" segments (due to the spline interpolation) and of "structured" segments (prescribed by neighbouring data points), which can lead to physically unreasonable variations of the density distribution, as will be discussed in the next section

2.2.3. computation of the electron density distribution

Following the procedure outlined in the previous sections, a FORTRAN subroutine has been written to reconstruct the electron density distribution from a given phase shift profile (see Appendix 5.2). The specific plasma geometry of CHS is taken into account by using equation (3) for the path lengths, and the calibration factor makes allowance for the fact that the HCN laser beams (λ = 0.337 mm) of the interferometer traverse the plasma twice. Taking the $\Delta\varphi$-profile of Fig. 8, one obtains the electron density distribution shown in Fig. 9. Note that the abscissa is not a space co-ordinate but gives the minor axis a of a contour line as described in section 2.2.1 (see inserted illustration in fig.9). In order to convert the abscissa into a more common surface label ρ, one may use the area A within a surface and express it with the help of equation (2) as $A= \pi\rho^2 = \pi ab = \pi a^2\, 1.02 \exp(0.036\, a)$, which leads to the transformation formula.

$$\rho = a\sqrt{1.02 \cdot \exp(0.036 \cdot a)} \tag{4}$$

The sharp local minima in the n_e-profile at $a \approx 6$ cm and $a \approx 9$ cm appear to be rather unrealistic. They are due to the non-monotonic slope of the $\Delta\varphi$-profile as prescribed by the closely spaced data points. However, keeping in mind that the experimental data were measured in a series of discharges, it is clear that slight irreproducibility and residual noise give rise to some scatter. In order to check the effect on the electron density distribution, the curve in Fig. 9 has been smoothed, and the phase shifts have been re-calculated for the modified n_e-profile (a FORTRAN routine is given in Appendix 5.3; the program has been tested by using the original profile, which results in a complete reproduction of the spline interpolation shown in Fig. 8). As can be seen in the lower part of Fig. 10, even a strong smoothing causes only minor deviations from the experimental points. So, unless the error bars are extremely small, one has to be very cautious to draw firm conclusions on small-scale variations of the density profile (such as local minima or a flat "shoulder").

Unfortunately, it is difficult to assess the actual error margins of the experimental data. To make a rough estimate we may use the scatter of the normalised time traces measured in the fixed upper channel at $z = +9.3$ cm (cf. Fig. 4). A blow-up for the time interval from 100 to 120 ms shows a "bandwidth" of 40 degrees, whereas the modulation amplitudes of the individual traces are 25 degrees or less (see Fig. 11). Therefore, as a lower limit we obtain an uncertainty of ±10 degrees, which is equal to the maximum deviation from the calculated phase shift profiles in Fig. 10.

2.3. Temporal evolution of the density profile

In order to establish a possible relation between the onset of MHD activity and the global shape of the electron density distribution, the evolution of the n_e-profile during the discharge has been investigated. Figure 12 shows the signals of the central channel ($z = \pm 0.0$) and of the channel at $z = -5.3$ cm, which were measured simultaneously in the same shot. In the early times of plasma build-up ($t < 50$ ms) and during plasma decay ($t > 125$ ms) the difference $\Delta\varphi(\pm 0.0) - \Delta\varphi(-5.3)$ is close to zero, although the central beam covers a longer path inside the plasma than the probing beam at $z = -5.3$ cm. Consequently, the density distribution must be rather flat or even hollow in these phases of the discharge.

To study the global profile evolution in more detail, the combined data of the "typical" discharge (Fig. 4) have been Abel-inverted in time steps of 20 ms (the sawtooth-like signal oscillations have been eliminated by taking time-averaged values for an interval of 5 ms). Using a spline interpolation of the experimental points, we obtain n_e-profiles with very pronounced fine-scale structures (see the dashed lines in Fig. 13), which we smooth out by applying the procedure described in the previous section. It must be emphasised, though, that this action involves a certain degree of arbitrariness and that, therefore, caution is advisable in interpreting details of the calculated electron density distribution.

Considering the unsmoothed n_e-profiles in Fig. 13, we notice that the fine-scale structures persist throughout the whole discharge without major changes. Hence they cannot be caused by a statistical scatter of the experimental data points but must be due to systematic reasons. A possible explanation based on instrumental effects might be a slight uncertainty in the exact position of the moved probing beam, which would introduce additional horizontal error bars. This supposition is corroborated by the fact that in shot #72226 the signals of the moved beam and of the fixed beam differ by a few percent, although for this discharge both beams were in symmetric positions relative to the horizontal midplane ($z = \pm 9.3$ cm). Unfortunately, a final conclusion cannot be drawn on the basis of the presently available data.

Concerning a possible dependence of the MHD activity on the global shape of the density profile, it appears – with the *caveat* emphasised before – that the onset of MHD oscillations during plasma build-up at $t \approx 60$ ms is related to a transition of the profile shape from hollow to peaked. The sharp decay of the plasma at $t > 120$ ms causes the profile to become hollow again, and the oscillations disappear.

3. Profile Changes during MHD Activity

3.1. Oscillatory behaviour of line-integrated data

So far we have concerned ourselves with the macroscopic features of the electron density distribution (specifically the temporal evolution during the discharge) and disregarded the oscillatory behaviour during MHD activity by forming an appropriate time average of the experimental data. Now we want to take a closer look at the periodic profile modifications induced by these effects. For this purpose we split the measured phase shift signals into three components corresponding to different temporal resolutions:

$$\Delta\varphi(z,t) = \Delta\varphi_1(z,\bar{\bar{t}}) + \Delta\varphi_2(z,\bar{t}) + \Delta\varphi_3(z,t) \quad (5)$$

The first term $\Delta\varphi_1$ contains all frequencies below ~150 Hz and gives just the global time evolution of the signal during the discharge. This part has been discussed in the previous sections. The next term $\Delta\varphi_2$ adds the frequency components between ~150 and ~750 Hz. It is still a time average of fast signal oscillations but resolves the periodic burst character of the MHD activity. Finally, the third term $\Delta\varphi_3$ covers the remaining frequency components from ~750 Hz to 12 kHz (frequencies beyond 12 kHz are excluded to reduce instrumental noise as described in section 2.1.1).

The sum of the first two terms provides information on the burst events but "smears out" the details contained in $\Delta\varphi_3$. The sum $(\Delta\varphi_1 + \Delta\varphi_2)$ may, therefore, be regarded to represent the $m = 0$ mode pattern of the density profile during a burst and can be treated by Abel-inversion on a system of contour lines of fixed shape (see section 2.2). By contrast, the fast oscillatory signal component $\Delta\varphi_3$ is most likely due to a combination of local density variations and deformations of the contour lines (corresponding to higher-order perturbations of the magnetic field structure). A clear separation of both effects would only be possible if measurements could be made under different angles of observation. However, the available data are limited to horizontal lines of sight. So we have to resort to model calculations and simulate the measured signals under more or less reasonable assumptions in order to extract some information on rapid profile changes.

3.1.1. combination of different shots

The data to be analysed were taken in a series of discharges with the movable probing beam in different positions. Consequently, the burst events are not correlated in time and have to be adjusted relative to each other on a common time axis. For this purpose we use the signals measured in the fixed probing beam ($z = +9.3$ cm) and select a time interval of 5 ms in each shot, which contains a typical burst (see Fig. 14). Next, we align these segments as shown in the left column of Fig. 15 to synchronise the events. Finally we plot the signals of the moved channel for the same segments and alignment to obtain a data set for a representative burst phenomenon (right column of Fig. 15; the red lines are the measured signals after removal of high-frequency noise (> 12 kHz); the black lines are the signals after low-pass filtering with a cut-off frequency of ~750 Hz, i.e. they represent the sum $(\Delta\varphi_1 + \Delta\varphi_2)$ as described above).

3.1.2. amplitude and phase relations among different lines of sight

The amplitudes and phases of the filtered signals (black lines) and of the fast oscillations (red lines) in fig.15 are determined in relation to the corresponding data of the fixed channel. In a first step, relative amplitudes $A_{\mathrm{mov}}(z)/A_{\mathrm{fix}}(z)$ are calculated for each shot. Then, in order to obtain absolute values and to eliminate shot-by-shot variations, these data are multiplied by the amplitude $A_{\mathrm{fix}}{}^*$ measured in a representative discharge (shot #72234). For the phases we find that the signals of the moved channel are shifted by 180° relative to the signals of the fixed channel, if $z < 7$ cm, and that they are unshifted for $z > 7$ cm. The results are plotted in Fig. 16 for the peak-to-peak amplitudes as a function of beam position. It is interesting to note that the filtered and unfiltered oscillations have a very similar dependence on z with the node being at the same position ($z_{\mathrm{node}} = 7$ cm).

From the fact that the outer channels ($z > 7$ cm) are strictly in phase with the fixed channel, which traverses the opposite part of the plasma cross-section, it must be concluded that the perturbation is dominated by a mode with even poloidal mode number m. However, the central part of the curves in Fig. 16 ($z < 5$ cm) does not conform to the standard pictures of a $m=0$ or a $m=2$ mode. To illustrate the characteristic features of these modes, Fig. 17 shows the results of simple model calculations. The upper part ($m = 0$) represents a periodic collapse of the whole plasma core, where the initially peaked profile is completely flattened, and the expelled electrons are re-distributed in the outer part of the plasma cross-section (this situation corresponds to a sawtooth crash in a tokamak discharge). The lower part is a simulation of a rotating $m=2$ island structure, where the plasma core region is squeezed by the two shaded areas, which mark flat regions in the density distribution. In both cases the maximum amplitude of the oscillating phase shift signals occurs for a probe beam passing through the plasma center ($z = 0$). In contrast to these models, the experimental data of Fig. 16 clearly show a decrease of the amplitude towards the center. Although the large gap between the data points puts a special weight on the central channel, the measurement is reliable because here data could be taken for each shot of the whole series.

3.2. Reconstruction of an "average" m = 0 *perturbation*

The mildly filtered signals (black lines in Fig. 15) resolve the periodic MHD burst events but "average out" the fast oscillations. Therefore they reflect the slow, global change of the electron density distribution and contain information on those regions of the plasma cross-section, which are mostly affected by a burst. These signals may be considered as being due to a $m=0$ perturbation, which causes a "symmetric" re-distribution of the electrons in the plasma cross-section without changing the shape of the contour lines. It must be clear, though, that a reconstruction of this "average" $m=0$ perturbation does not provide the true variation of the density profile, but is – in a certain sense – just a low-frequency Fourier component.

3.2.1. Abel inversion of the filtered data

We consider only the signal components $\Delta\varphi_2$, which contain the frequencies between ~150 and ~750 Hz (see Fig. 18 for an illustration). They oscillate with a peak-to-peak amplitude $A_{pp}(z)$ depending on the probing beam position. If we choose the times t_1 and t_2 as indicated in Fig. 18, we may plot two phase shift profiles $\Delta\varphi_2(z,t_1) = +A_{pp}(z)/2$ and $\Delta\varphi_2(z,t_2) = -A_{pp}(z)/2$ where $A_{pp}(z)$ is given by Fig. 16, and the node at $z = 7$ cm causes a change of the sign of A_{pp}. The profiles $\Delta\varphi_2(z,t_1)$ and $\Delta\varphi_2(z,t_2)$ can be inverted using the methods described in section 2.2. The resulting differential electron density distributions $\Delta n_e(t_1)$ and $\Delta n_e(t_2)$ are shown in Fig. 19.

In the lower part of Fig. 19 we have plotted $\overline{n_e} \pm \Delta n_e$, where $\overline{n_e}$ is the smooth density profile calculated in section 2.2 (heavily filtered signals; see Fig. 10). Before the MHD burst (time t_1) the electron density distribution is rather flat up to $a \cong 7$ cm. During the burst (time t_2) the density decreases on average in an annular zone (2 cm < a < 8 cm), and increases on average in the outer plasma region as well as in the very centre. Owing to large error bars of the measured amplitudes and to missing data between $z = 0$ and 5.3 cm, the apparent central increase and the local minimum at $a \cong 7$ cm during the burst may be artefacts of the inversion process. Nevertheless, it can be stated that the MHD burst phenomenon causes a significant deterioration of the electron confinement predominantly in a ring zone, but not in the whole plasma core.

3.3. Modelling of fast oscillations by rotating island structures

The fast signal oscillations during a MHD burst are nearly sinusoidal and have a period of $\tau \leq 0.4$ ms. If they were caused by a periodic $m=0$ perturbation, one would expect a sawtooth- like time behaviour reflecting a rapid loss of confinement (i.e. a fast local flattening of the density profile) and a comparatively slow restoration of the density gradient, for which the time $\tau/2 \cong 0.2$ ms would hardly be sufficient. It is, therefore, more likely to attribute the fast oscillations to a deformation of the density contours, which perform a poloidal rotation in the vacuum vessel at a frequency of a few kHz. The signal amplitudes (and hence the underlying MHD mode) show a rapid growth and a slow decay (see Fig. 14). Half-way into the burst, the amplitudes change on a time scale much longer than τ, thus indicating a quasi-stationary deformation. However, owing to the fixed non-circular shape of the plasma boundary, the deformed structure cannot rotate like a rigid body but will undergo a periodic compression and elongation (for a schematic illustration see the $m=2$ case sketched in Fig. 17). Clearly, the available experimental data are insufficient to reveal these details unambiguously, but we can try to gain some qualitative insight by modelling the characteristic features of the measured signals under more or less realistic conditions.

3.3.1. model assumptions

The simplest model, which is in rough accordance with the amplitude and phase relations of the observed signals, is a $m=2$ perturbation comprising two crescent-shaped flat regions ("islands") as indicated by the shaded areas in Fig. 17. If we allow such an island structure to rotate and "smear out" periodic local variations by forming an average over one revolution, we obtain a mean density distribution with a flattened ring zone as we found in the previous section. Since the structure is quasi-stationary with respect to radial expansion, there is little net transport across the deformed magnetic surfaces. Hence, we keep the total number of electrons constant within the squeezed plasma core, and we assume that the plasma boundary is not affected by the rotating islands. Furthermore, we simplify the plasma geometry by using two sets of concentric ellipses to fix the density contours in the boundary and core region, respectively, and we take the density profile to be completely flat inside the two opposite islands. With these assumptions our model distribution has a form as shown in Fig. 20: the outer zone and the islands make up a rigid pedestal, on top of which rests a rotating peak that touches the edge of the plateau at two opposite points. Because we are interested in the oscillating part of the signals only, we can ignore the pedestal and limit our calculations to the phase shifts caused by the peak.

Due to the elliptical shape of the pedestal, the distance between the X-points (i.e. the points of contact of the rotating plasma core with the edge of the pedestal) depends on the rotation angle. If we keep the core elongation fixed, the area within a given contour will decrease when the X-points move from a horizontal to a vertical position. On the other hand, since we expect little transport across the contour lines within one period of rotation, we require the total number of electrons in the core to be unchanged. In order to satisfy this condition, we have to keep constant the product of density and area within a ring zone.

Our simulation program allows us to treat two different models: (a) the case of fixed area and density by matching the elongation, and (b) the case of fixed elongation and variable area by matching the electron density (for details see Appendix 5.5; the calculation of the path length for a probing beam intersecting a tilted ellipse is described in Appendix 5.4). A FORTRAN subroutine to compute the phase shift $\Delta\varphi$ as a function of the rotation angle α can be found in Appendix 5.6. It requires as input information (i) the position z of the horizontal probing beam, (ii) the minor and major semi-axes A and B of the elliptical pedestal, (iii) the electron density distribution $n_e(i)$ in the ring zones (where $i = 1 \ldots n$ from centre to edge), and (iv) the prescribed area $f = a \cdot b = F/\pi$ of the contour containing the X-points (model (a)) or the prescribed ellipticity ε of the plasma core (model (b)). The data are written into an output array $(\alpha_j, \Delta\varphi_j)$ for $0° \le \alpha_j \le 90°$ in steps of 1°.

3.3.2. comparison with experimental data

In order to adapt our model to the experimental conditions, we choose a pedestal with a major axis $B = 18$ cm and a minor axis $A = B/\sqrt{2} =$ 12.7 cm. The ratio $B/A = \sqrt{2}$ conforms to the elongation of a corresponding flux surface in CHS (see Fig. 7), and the choice of A accounts for the fact that the pedestal cannot extend much beyond $z = 11.6$ cm, because the signals measured at this beam position and further outward show little or no modulation. To select an appropriate elongation and size of the rotating plasma core, we argue that the major axis b is continuously decreasing for α going from 0° to 90°, while the minor axis a must increase to keep the area $F = \pi ab$ constant (our model requires that $b(\alpha{=}0°) = B$ and $b(\alpha{=}90°) = A$). Following the derivation of $b(\alpha)$ in Appendix 5.5, it can be shown that the condition $a(\alpha) \le b(\alpha)$ has to be satisfied. So, for the maximum possible area, we have $a(90°) = b(90°)$ and hence $f = [b(90°)]^2 = B^2/2$. Taking this value, we find for $\alpha = 0°$ an ellipticity of $\varepsilon = a_0 / b_0 = f / b_0^2 = ½$, which we use for our calculations according to model (b). Fig. 21 shows a scaled drawing of the rotating structure inside the cross-section of CHS.

For the electron density in the ring zones of the plasma core we assume either a peaked or a hollow distribution (right part of Fig. 21; in model (b) we use a scaling factor inversely proportional to the area $f(\alpha) = \varepsilon\,[b(\alpha)]^2$ in order to keep the total number of electrons fixed). The calculations are performed for the same probing beam positions as in the experiment.

Figures 22 and 23 show the results of the model calculations for a peaked and a hollow density profile, respectively. The simulated phase shifts are plotted versus the rotation angle α for a full revolution of the plasma core. For comparison, a set of experimental data is also shown, where the time axes for the different traces have been adjusted as described in section 3.1.1. Irrespective of the density distribution, model (a) produces signals of nearly trapezoidal shape, whereas the signals resulting from model (b) are much closer to the sinusoidal shape observed in the experiment. We can, therefore, conclude that the rotating plasma core largely retains its elongation, while the island width undergoes a fairly strong modulation. With respect to the density profile, we obtain closer agreement between measurement and simulation by using the hollow distribution. Characteristic features like the change of amplitude as a function of beam position and the location for phase reversal are much better reproduced in Fig. 23 than in Fig. 22. As a matter of fact, the coincidence of measured and calculated signals is surprisingly high in view of our crude model, and the remaining discrepancies could probably be further reduced by some fine-tuning of the input parameters.

Nevertheless, there are contradictions to the previous reconstruction of an "average" $m=0$ perturbation (section 3.2.). In our model the island covers for $\alpha = 0$ the distance between 9 cm and 12.7 cm along the vertical diameter. Consequently, the "average" density profile should have a "shoulder" (i.e. a local indentation) predominantly in this range. However, the distribution shown in Fig. 19 (blue curve) has its flat part between 6 cm and 10 cm. Furthermore, the "average" profile is peaked in the center, whereas in our model a hollow distribution provides a much better fit to the oscillatory part of the measured signals.

4. Summary and Conclusions

In this report an attempt is made to gain insight into spatial and temporal changes of the electron density under discharge conditions of repetitive MHD activity in the CHS heliotron/ torsatron device. The investigation is solely based on experimental data provided by a HCN laser interferometer comprising three horizontal probing beams, one of which could be moved between shots. By combining the signals of a series of reproducible discharges, a set of phase shifts $\Delta\varphi(z) \propto \int_{L(z)} n_e\, ds$ along twelve different chords $L(z)$ through the plasma cross-section has been compiled and used for the analysis.

In a first step, these signals were low-pass filtered to completely smooth out periodic MHD-induced effects, and the global temporal evolution of the density distribution was determined by means of a generalised Abel inversion technique. It was found that in the early times of plasma build-up ($t < 50$ ms) and during plasma decay the density profile is rather flat or even hollow. The onset of the MHD activity appears to be correlated with the transition of the profile shape from hollow to peaked.

Next, the cut-off frequency of the low-pass filter was raised such that the periodic burst events could be resolved but the related fast oscillations were still "averaged out". The analysis (again by Abel inversion) of these data immediately before and during a burst revealed that the MHD activity causes on average a deterioration of the electron confinement in a ring zone of the cross-section, but not in the whole plasma core.

Finally, in order to clarify the nature of the fast signal oscillations in a burst, a simple m=2 perturbation model was used to simulate the experimental data. The model assumes an electron density distribution consisting of a rigid pedestal, on top of which rotates a squeezed peak. By choosing a hollow density profile for the rotating peak and keeping its elongation fixed during one revolution, a fairly close fit to the oscillatory parts of the measured signals has been obtained.

Unfortunately, some of the features of the pedestal model (in particular, the location of the crescent-shaped islands and the hollowness of the core distribution) are inconsistent with the findings for the "average" profile change during a MHD burst. In principle, this situation can be amended by developing a more advanced model (possibly by taking into account the true shape of the flux surfaces and allowing for contributions of higher-order perturbations with even mode number m). On the other hand, any sophistication of the simple pedestal model increases the number of free parameters at the expense of unambiguity, unless additional information provided by other diagnostics can be incorporated. For example, a detailed analysis of the Mirnov oscillations might indicate the presence and relative strength of higher-order perturbations, and time and space resolved measurements of the electron temperature and the soft x-ray emission could help to determine the shape and size of the rotating core structure. In addition, for the CHS device rather unique information about the electrostatic potential profile under very similar discharge conditions is available, and it is certainly rewarding to use these data for a detailed comparison – not only to improve the knowledge about the density distribution but also to correlate potential and density fluctuations for the purpose of transport analyses.

References

[1] A. Fujisawa *et al.*, Proc. 16th Int. Conf. on Fusion Energy (Montreal, 1996), Vol. 2, p. 41, IAEA, Vienna 1997

[2] K.Tanaka et al., Rev. Sci. Instrum. Vol.70, p.730 1999

[3] Y.Jiang et al., Rev. Sci. Instrum. Vol.68, p.902 1997

5. Appendix

5.1. removal of phase jumps in the interferometric signals

```
!****************************************************************************
!  SUBROUTINE: JUMP
!
!  PURPOSE:   Eliminate overflow of phase detector and adjust base line to zero
!****************************************************************************
          subroutine JUMP(signal,ndata)

          implicit none

        integer i,j,k,ndata                    ! ndata  = number of data points in input/output array
          real signal(ndata)                   ! signal = phase shift data
        real vor                               ! vor      = offset prior to plasma ignition

        do 1 j=1,ndata-1
                  if ((signal(j+1)-signal(j)).gt.250.) signal(j+1)=signal(j+1)-360.
                  if ((signal(j+1)-signal(j)).gt.-90.) goto 1
                  do 2 k=1,20
                            signal(j+1)=signal(j+1)+360.
                            if ((signal(j+1)-signal(j)).gt.-90.) goto 1
2                 continue
1         continue

          vor=0.0                              ! calculate average phase shift for the first 300 data points
          do i=1,300
                  vor=vor+signal(i)
          enddo
          vor=vor/300.
          do j=1,ndata                         ! subtract offset from phase shift data
                  signal(j)=signal(j)-vor
          enddo

          end subroutine JUMP
```

5.2. calculation of the density distribution for a given phase shift profile

```
!******************************************************************************
!  SUBROUTINE: INVERS
!
!  PURPOSE:   inversion of phase shift profile for special geometry of CHS
!                  (calibration factor „fac“ valid for wavelength of HCN laser and double beam path)
!******************************************************************************
        subroutine INVERS(x,y,a,nx)

          implicit none

          integer nx                      ! nx = number of data points in phase shift profile
        integer i,j,k
          real x(nx)                      ! x     = abscissa of phase shift profile (input)
        real y(nx)                        ! y     = phase shift data (input)
        real a(nx)                        ! a     = electron density in ring zones (output)
          real ac,bc,f,xs,sum,h1,h2,zo,zu,fac
          parameter (ac=2.04,bc=0.036,fac=0.092)

          f=fac*(y(nx)+y(nx-1))/2.             ! calculate local value in outermost zone
          xs=(x(nx)+x(nx-1))/2.
          h1=ac*exp(bc*x(nx))
          zo=h1*sqrt(x(nx)**2-xs**2)
          a(nx-1)=f/zo
```

```
       do 1 i=nx-2,1,-1                    ! calculate local values in zones by
             f=fac*(y(i+1)+y(i))/2.        ! progressing from ouside to center
             xs=(x(i+1)+x(i))/2.
             sum=0.0
             do 2 k=nx-1,i+1,-1
                   h1=ac*exp(bc*x(k+1))
                   zo=h1*sqrt(x(k+1)**2-xs**2)
                   h2=ac*exp(bc*x(k))
                   zu=h2*sqrt(x(k)**2-xs**2)
                   sum=sum+a(k)*(zo-zu)
2            continue
             h1=ac*exp(bc*x(i+1))
             zo=h1*sqrt(x(i+1)**2-xs**2)
             a(i)=(f-sum)/zo
1      continue

       end subroutine INVERS
```

5.3. calculation of the phase shift profile for a given density distribution

```
!*******************************************************************************
!  SUBROUTINE: PHASCOMP
!
!  PURPOSE: calculation of phase shift profile for a given density distribution in geometry of CHS
!                    (calibration factor „con“ valid for wavelength of HCN laser and double beam path)
!*******************************************************************************
      subroutine PHASCOMP(x,ne,phas,nx)

       implicit none

       integer nx                   ! nx = number of data points in phase shift profile
       integer in,ip
       real x(nx)                   ! x     = abscissa of electron density profile (input)
      real ne(nx)                   ! ne = electron density data (input)
      real phas(nx)                       ! phas = phase shift data (output)
       real con,ac,bc,fac,delx,deln,a,xp
       parameter (con=10.89,ac=2.04,bc=0.036)

       delx=x(2)-x(1)
       do 1 in=1,nx-1
             deln=ne(in)-ne(in+1)
             a=x(in)+delx/2.
             fac=con*ac*exp(bc*a)
           phas(in)=0.0
             do 2 ip=1,in
                   xp=x(ip)-delx/2.
                   phas(ip)=phas(ip)+fac*deln*sqrt(a*a-xp*xp)
2            continue
1     continue
      phas(nx)=0.0

       end subroutine PHASCOMP
```

5.4. *calculation of the chord length L*

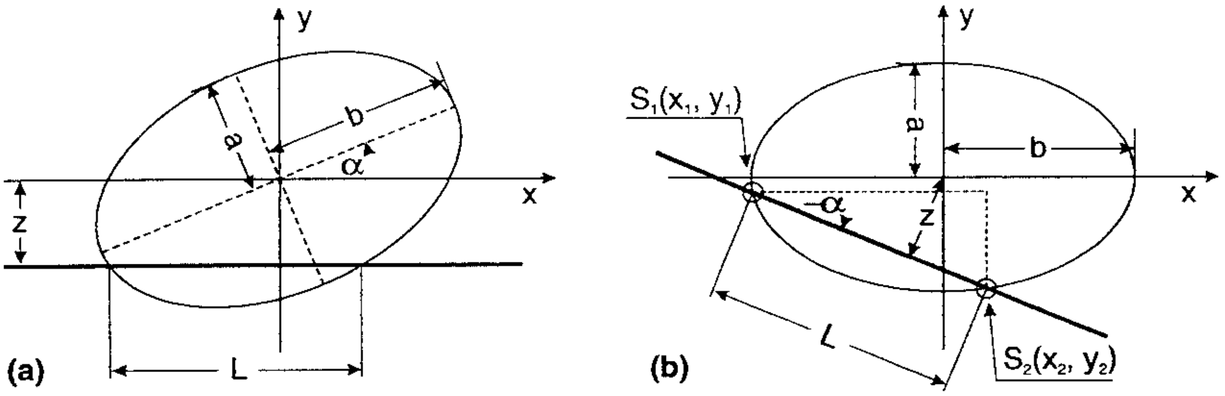

Consider a tilted ellipse with semi-axes b and $a = \varepsilon b$ according to subfigure (a), which is intersected by a horizontal line at a distance z from the origin. If we rotate the graph by the angle $-\alpha$ as shown in subfigure (b), we can express the ellipse as

$$\frac{x^2}{b^2}+\frac{y^2}{a^2}=1 \quad\Rightarrow\quad y=\varepsilon\sqrt{b^2-x^2} \quad (\text{where } \varepsilon=a/b),$$

and the line is given by

$$y=-x\cdot\tan\alpha-\frac{z}{\cos\alpha}=\frac{-x\cdot\sin\alpha-z}{\cos\alpha}.$$

For the intersection points S_1 and S_2 we have

$$\varepsilon\sqrt{b^2-x_s^2}\cos\alpha=-(x_s\sin\alpha+z).$$

Solving this equation for x_s yields

$$x_{1,2}=\frac{-z\sin\alpha\pm\varepsilon\cos\alpha\sqrt{b^2(\sin^2\alpha+\varepsilon^2\cos^2\alpha)-z^2}}{\sin^2\alpha+\varepsilon^2\cos^2\alpha}.$$

From the shaded triangle in subfigure (b) we find immediately

$$\cos\alpha=\frac{x_2-x_1}{L} \quad\Rightarrow\quad L=\frac{x_2-x_1}{\cos\alpha},$$

and by combining the last two equations, we obtain the result

$$L(z,b,\varepsilon,\alpha)=\frac{2\varepsilon\sqrt{b^2(\sin^2\alpha+\varepsilon^2\cos^2\alpha)-z^2}}{\sin^2\alpha+\varepsilon^2\cos^2\alpha}.$$

```
!*****************************************************************************
!  FUNCTION: CL
!
!  PURPOSE:   calculation of chord length in tilted ellipse
!*****************************************************************************
        function cl(z,alph,eps,bax)

        implicit none

        real z              !chord distance from origin
        real alph           !rotation angle [rad]
        real eps            !ellipticity a_axis/b_axis
        real bax            !major semi-axis of ellipse
        real cl             !chord length
        real aux1,aux2

        cl=0.0
        aux1=sin(alph)*sin(alph)+eps*eps*cos(alph)*cos(alph)
        aux2=bax*bax*aux1-z*z
        if (aux2.gt.0.0) cl=2.*eps*sqrt(aux2)/aux1

        return
        end function cl
```

5.5. calculation of the axis b

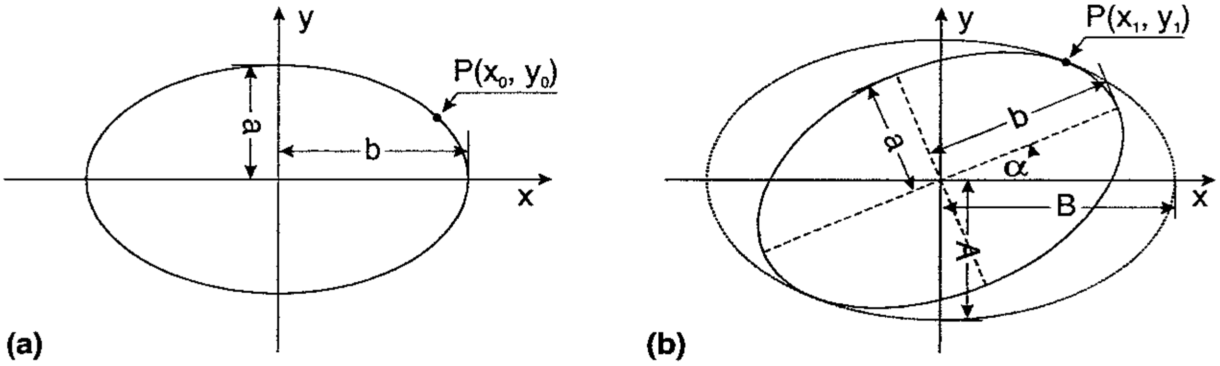

In our model, the contour lines of the plasma core are ellipses which rotate on a static pedestal. Because the outermost of these contours always touches the edge of the pedestal, the length b is a function of the rotation angle α. For a given pedestal (axes A and B) and for a fixed ellipticity $\varepsilon = a/b$ of the rotating contour we want to determine the axis $b(\alpha)$.

Consider a fixed point P on the ellipse. For $\alpha = 0$ (subfig. (a)) this point satisfies the equation

$$\frac{x_0^2}{b^2} + \frac{y_0^2}{a^2} = 1 \quad \Rightarrow \quad y_0 = \varepsilon\sqrt{b^2 - x_0^2} \quad (\text{where } \varepsilon = a/b).$$

A rotation of the ellipse by the angle α (subfig. (b)) moves P to the co-ordinates

$$x_1 = x_0 \cos\alpha - y_0 \sin\alpha \qquad \text{and} \qquad y_1 = x_0 \sin\alpha + y_0 \cos\alpha .$$

If P is the point of contact with the pedestal (outer ellipse), then it has to satisfy the condition

$$\frac{x_1^2}{B^2} + \frac{y_1^2}{A^2} = 1 .$$

Combining all these formulas, we obtain

$$\frac{\left(x_0\cos\alpha-\varepsilon\sqrt{b^2-x_0^2}\,\sin\alpha\right)^2}{B^2}+\frac{\left(x_0\sin\alpha+\varepsilon\sqrt{b^2-x_0^2}\,\cos\alpha\right)^2}{A^2}=1,$$

which we can solve for x_0:

$$(x_0^2)_{1,2}=\frac{v^2b^2-2u\xi\pm\sqrt{(v^2b^2-2u\xi)^2-4(u^2+v^2)\xi^2}}{2(u^2+v^2)}$$

$$\text{where: }\begin{cases}u=B^2(\sin^2\alpha-\varepsilon^2\cos^2\alpha)+A^2(\cos^2\alpha-\varepsilon^2\sin^2\alpha)\\ v=2\varepsilon(B^2-A^2)\,\sin\alpha\,\cos\alpha\\ \xi=\varepsilon^2(B^2\cos^2\alpha+A^2\sin^2\alpha)b^2-A^2B^2=w\cdot b^2-s\end{cases}$$

Because we want P to be a point of contact and not a point of intersection of the two ellipses, the root must be zero:

$$(v^2b^2-2u\xi)^2-4\xi^2(u^2+v^2)=0\,.$$

Replacing the quantities u, v and ξ, we can solve this equation for b and arrive at

$$b(\alpha,\varepsilon,A,B)=\sqrt{\frac{1}{2\varepsilon^2}\left[u+2w-\sqrt{u^2+v^2}\right]}$$

$$\text{where: }\begin{cases}u=B^2(\sin^2\alpha-\varepsilon^2\cos^2\alpha)+A^2(\cos^2\alpha-\varepsilon^2\sin^2\alpha)\\ v=2\varepsilon(B^2-A^2)\,\sin\alpha\,\cos\alpha\\ w=\varepsilon^2(B^2\cos^2\alpha+A^2\sin^2\alpha)\end{cases}$$

For reasons explained in section 3.3.1. it may be more realistic, not to prescribe the ellipticity $\varepsilon=a/b$ of the rotating contour but to keep the area $F=\pi ab=\pi\varepsilon b^2$ constant during the rotation. In that case, we have to substitute the ellipticity by $\varepsilon=f/b^2$, where $f=F/\pi$. After some algebra we obtain:

$$b(\alpha,f,A,B)=\sqrt{\frac{\rho+\sqrt{\rho^2-4f^2\sigma\tau}}{2\sigma}}$$

$$\text{where: }\begin{cases}\rho=A^2B^2+f^2\\ \sigma=B^2\sin^2\alpha+A^2\cos^2\alpha\\ \tau=B^2\cos^2\alpha+A^2\sin^2\alpha\end{cases}$$

```
!***************************************************************************
!  FUNCTION: BAX1
!
!  PURPOSE:  calculation of semi-axis of circumscribed, tilted ellipse      (prescribed ellipticity)
!***************************************************************************
        function bax1(alph,eps,aa,bb)

        implicit none
        real alph            !rotation angle [rad]
        real eps             !ellipticity a_axis/b_axis
        real aa              !minor semi-axis of outer ellipse
        real bb              !major semi-axis of outer ellipse
        real bax1  !major semi-axis of tilted inner ellipse
        real aux1,aux2,u,v,w

        bax1=0.0
        aux1=sin(alph)*sin(alph)-eps*eps*cos(alph)*cos(alph)
        aux2=cos(alph)*cos(alph)-eps*eps*sin(alph)*sin(alph)
        u=bb*bb*aux1+aa*aa*aux2
        aux1=2.*eps*sin(alph)*cos(alph)
        v=(bb*bb-aa*aa)*aux1
        aux1=bb*bb*cos(alph)*cos(alph)
        aux2=aa*aa*sin(alph)*sin(alph)
        w=eps*eps*(aux1+aux2)
        aux1=u*u+v*v
        if(aux1.gt.0.0)aux1=sqrt(aux1)
        aux2=u+2.*w-aux1
        if(aux2.gt.0.0) bax1=sqrt(aux2/(2.*eps*eps))

        return
        end function bax1


!***************************************************************************
!  FUNCTION: BAX2
!
!  PURPOSE:  calculation of semi-axis of circumscribed, tilted ellipse     (prescribed area)
!***************************************************************************
        function bax2(alph,f,aa,bb)

        implicit none
        real alph            !rotation angle [rad]
        real f               !area of ellipse divided by pi
        real aa              !minor semi-axis of outer ellipse
        real bb              !major semi-axis of outer ellipse
        real bax2  !major semi-axis of tilted inner ellipse
        real aux,r,s,t

        bax2=0.0
        r=aa*aa*bb*bb+f*f
        s=bb*bb*sin(alph)*sin(alph)+aa*aa*cos(alph)*cos(alph)
        t=bb*bb*cos(alph)*cos(alph)+aa*aa*sin(alph)*sin(alph)
        aux=r*r-4.*f*f*s*t
        if(aux.le.0.0)goto 10
        aux=(r+sqrt(aux))/(2.*s)
        if(aux.le.0.0)goto 10
        bax2=sqrt(aux)

10      return
        end function bax2
```

5.6. calculation of signal modulation (pedestal model)

```
!***************************************************************************
!  SUBROUTINE: PHASMOD
!
!  PURPOSE:   modulation of phase shift signal produced by rotating plasma core
!                         (calculation for rotation of 90 deg)
!                         (calibration factor FAC valid for double-pass HCN laser)
!***************************************************************************
        subroutine phasmod(z,a,b,ne,n,eps,f,model,phidat)

        implicit none

        real z                          !position of probe beam
        real a,b                        !minor and major axis of elliptical pedestal
        integer n                       !number of ring zones
        real ne(n)              !electron density in ring zones (i=1: center; i=n: edge)
        real eps                        !prescribed ellipticity of plasma core (model=1)
        real f                          !prescribed area of outermost rotating ellipse (model=2)
        integer model                   !fixed ellipticity OR fixed area
        real phidat(2,91)               !2-d array for phase shifts vs  rotation angle

        real fac,pi,adeg,arad,b0,f0,eps0,bd,dne,chord,phi,bax1,bax2,cl
        integer ia,id

        parameter (fac=10.89)           !ne in 10^13 cm^-3; path length in cm

        pi=2.*asin(1.)

        do 1 ia=1,91
                adeg=float(ia-1)
                phidat(1,ia)=adeg
                if(abs(z).ge.a)then
                        phidat(2,ia)=0.0
                        goto 1
                endif
                arad=(pi/180.)*adeg
                if(model.eq.1)then
                        b0=bax1(arad,eps,a,b)
                        eps0=eps
                        f0=eps*b0*b0
                else
                        b0=bax2(arad,f,a,b)
                        eps0=f/(b0*b0)
                        f0=f
                endif
                phi=0.0
                do 2 id=1,n
                        bd=float(n+1-id)*b0/float(n)
                        if(abs(z).ge.bd)goto 10
                        dne=ne(n)
                        if(id.gt.1) dne=ne(n+1-id)-ne(n+2-id)
                        chord=cl(z,arad,eps0,bd)
                        phi=phi+dne*chord
2               continue
10              phidat(2,ia)=fac*(f/f0)*phi
1       continue

        return
        end subroutine phasmod
```

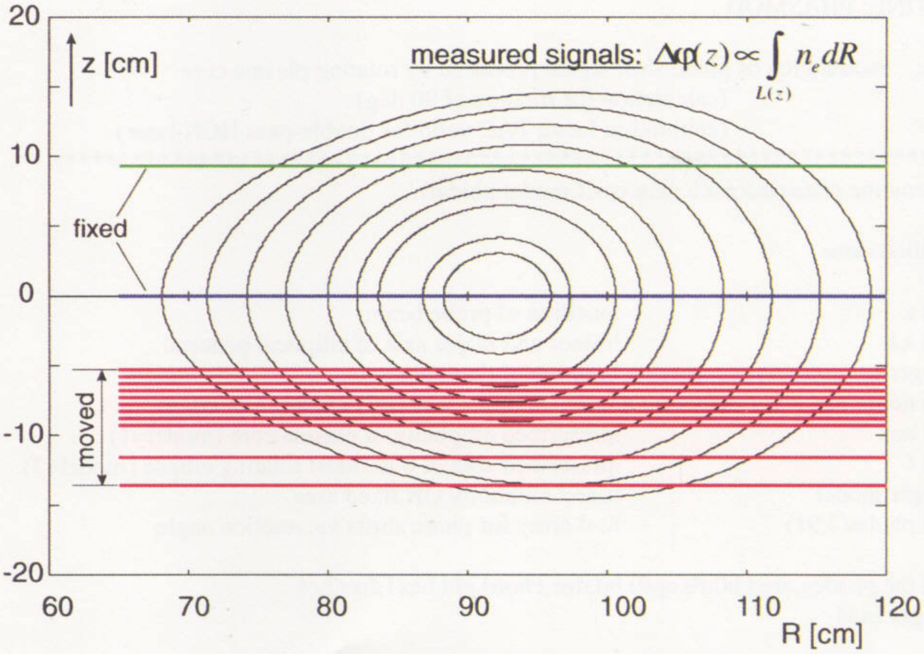

Fig. 1: *positions of the interferometric probing beams in the non-circular cross-section of CHS.*

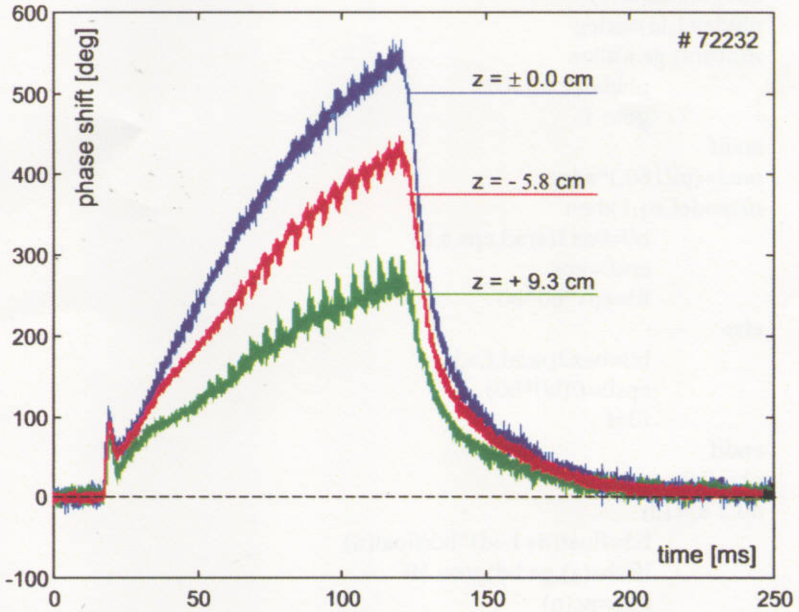

Fig. 2: *interferometric signals (after correction for phase jumps) measured in CHS shot #72232.*

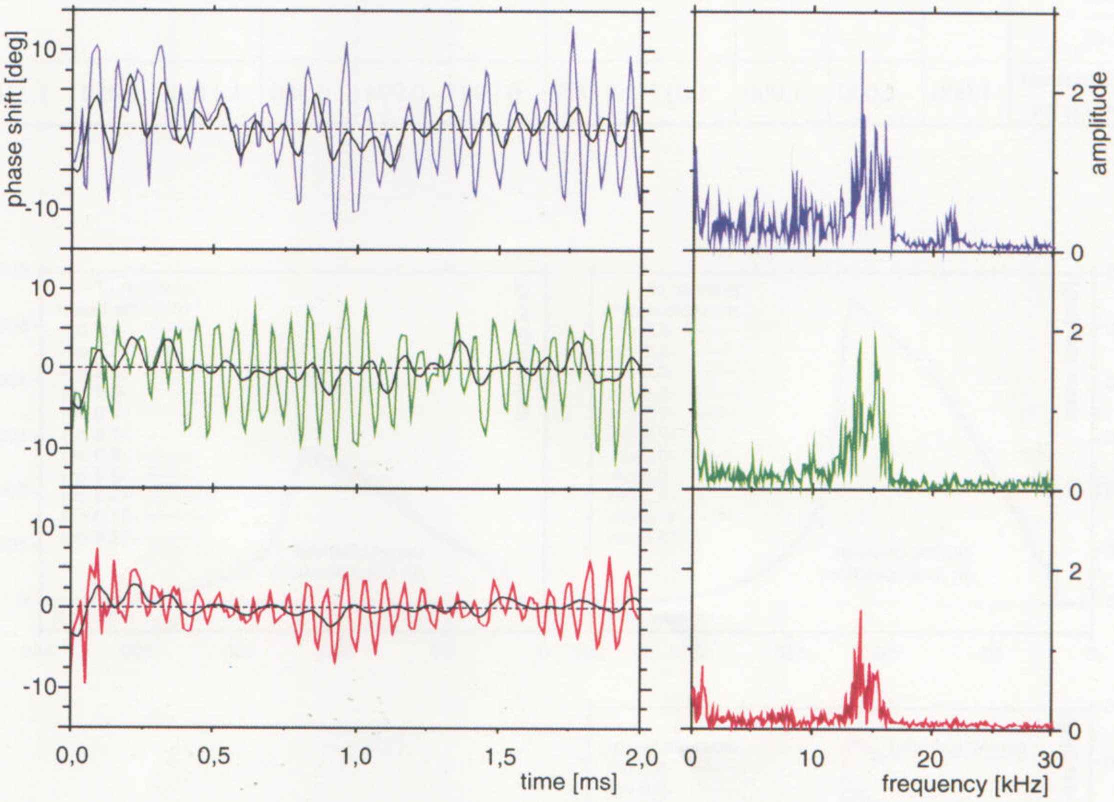

Fig. 3: *interferometric signals and their noise spectra before plasma ignition (CHS shot #72232).*

Shot number	72234	72232	72233	72235	72229	72236	72237	72238	72226	72230	72210
position of movable beam	-5.3	-5.8	-6.3	-6.8	-7.3	-7.8	-8.3	-8.8	-9.3	-11.6	-13.6
$\frac{\text{average phase shift}}{\Delta\varphi_{center}}$	483.7	484.6	484.0	476.0	445.9	487.2	488.0	504.1	433.5	461.2	369.3
normalisation factor	1.000	1.000	1.000	1.017	1.085	0.994	0.994	0.960	1.116	1.050	1.310

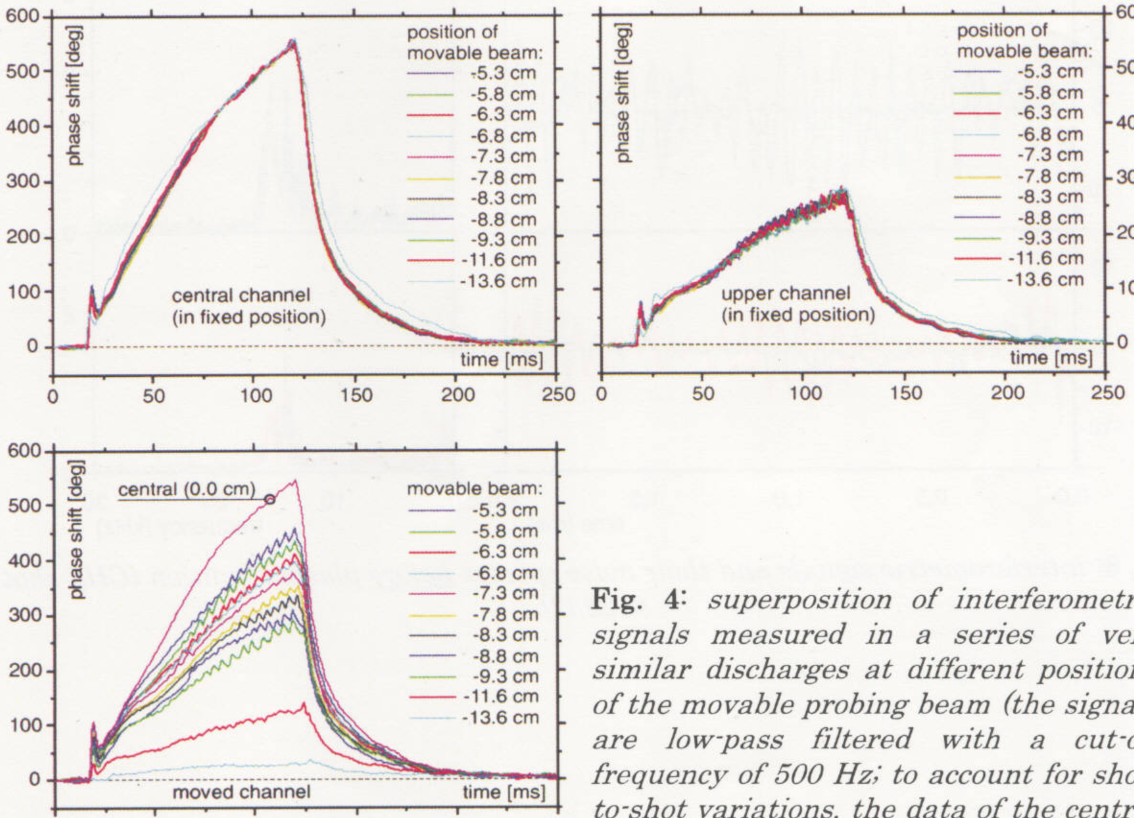

Fig. 4: *superposition of interferometric signals measured in a series of very similar discharges at different positions of the movable probing beam (the signals are low-pass filtered with a cut-off frequency of 500 Hz; to account for shot-to-shot variations, the data of the central channel are normalised in the time interval between 80 and 120 ms; for details see text).*

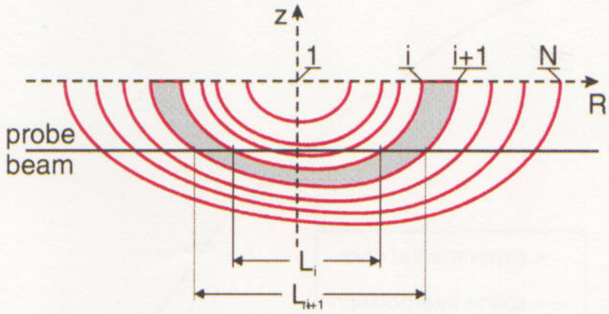

Fig. 5: *schematic drawing of the plasma cross-section in CHS with closely spaced magnetic surfaces (representing contour lines of constant electron density).*

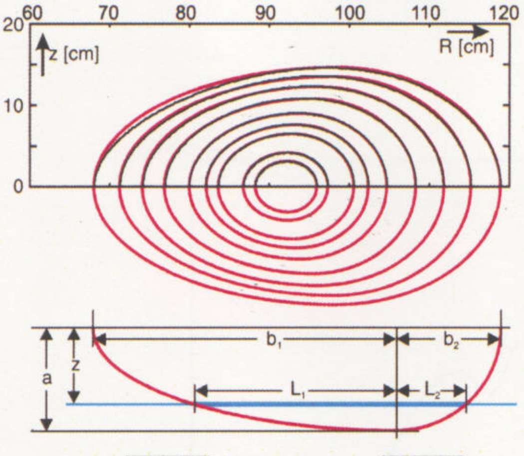

$$L_1 = b_1\sqrt{1-(z/a)^2} \quad \text{and} \quad L_2 = b_2\sqrt{1-(z/a)^2}$$

$$\Rightarrow \quad L = L_1 + L_2 = (b_1 + b_2)\sqrt{1-(z/a)^2}$$

Fig. 6: *approximation of elongated flux surfaces by two semi-ellipses with a common minor axis.*

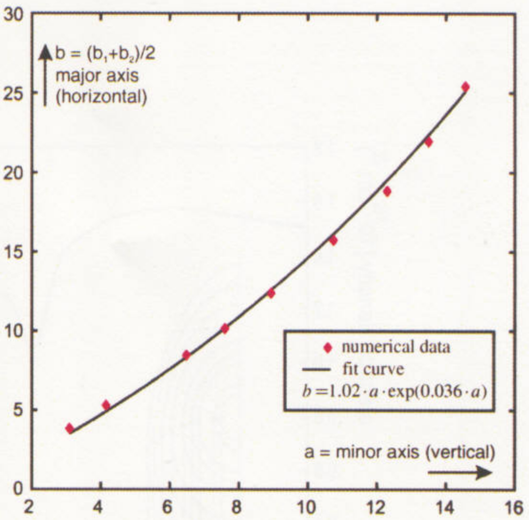

Fig. 7: *analytical fit to the horizontal elongation of the flux surfaces in CHS (vacuum field).*

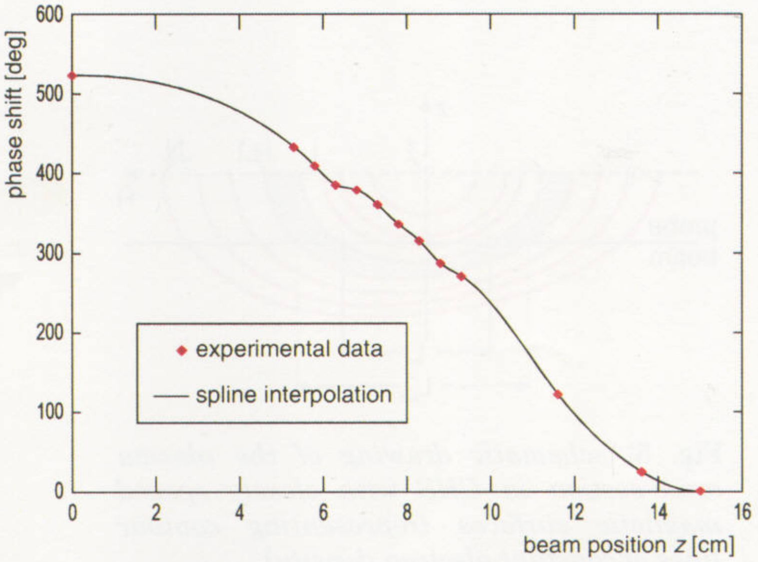

Fig. 8: *phase shift profile calculated by a spline interpolation of the experimental data (averaged over MHD activity in the time interval between 110 and 115 ms).*

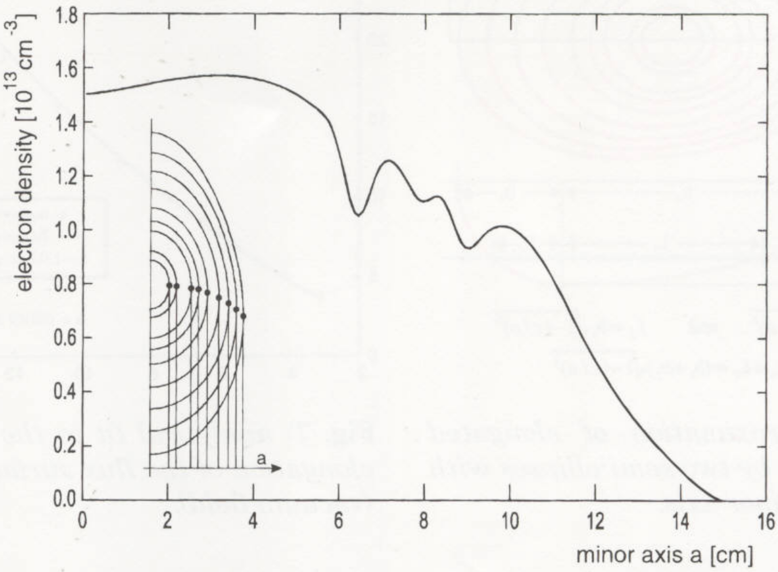

Fig. 9: *electron density distribution corresponding to the phase shift profile of Fig. 8.*

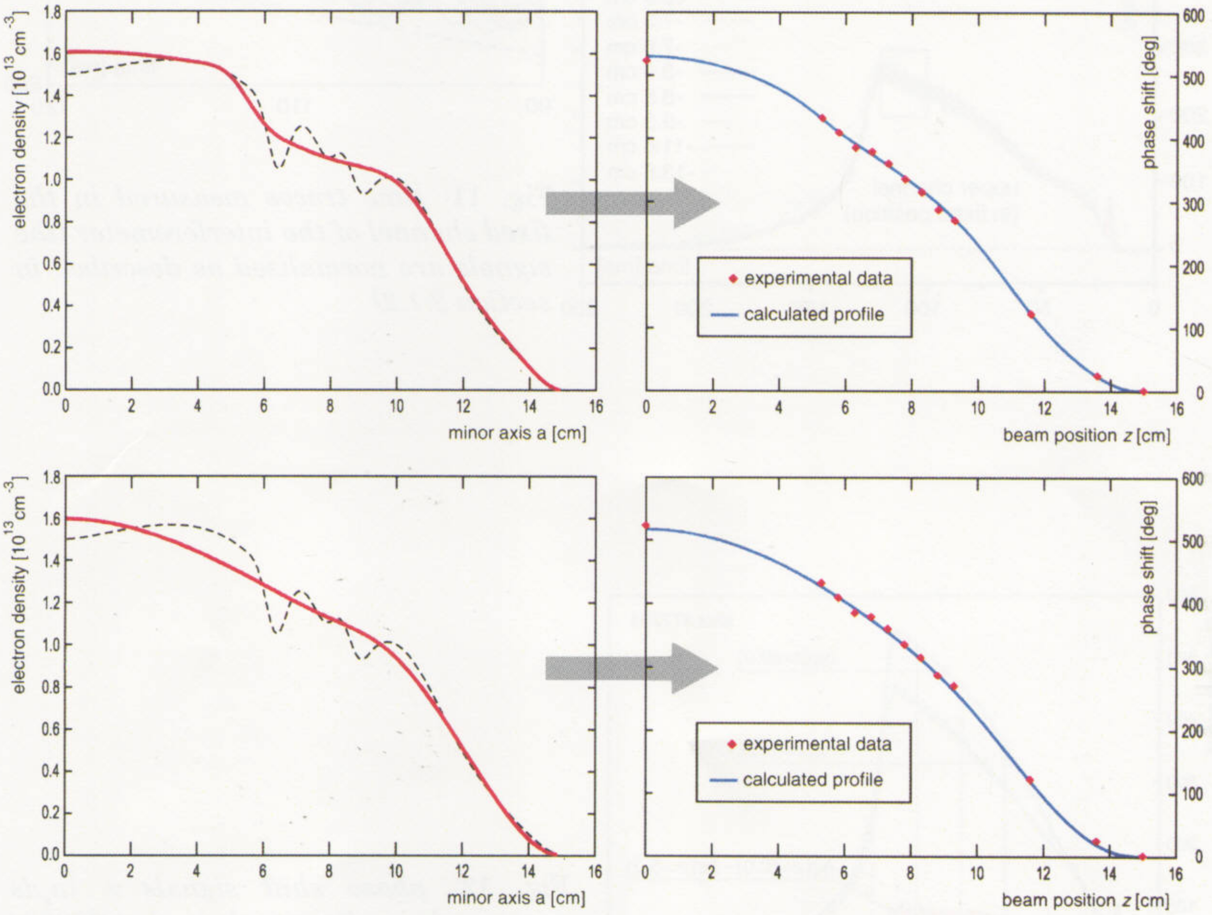

Fig. 10: *„smoothed“ electron density distributions (left) and re-calculated phase shift profiles (right).*

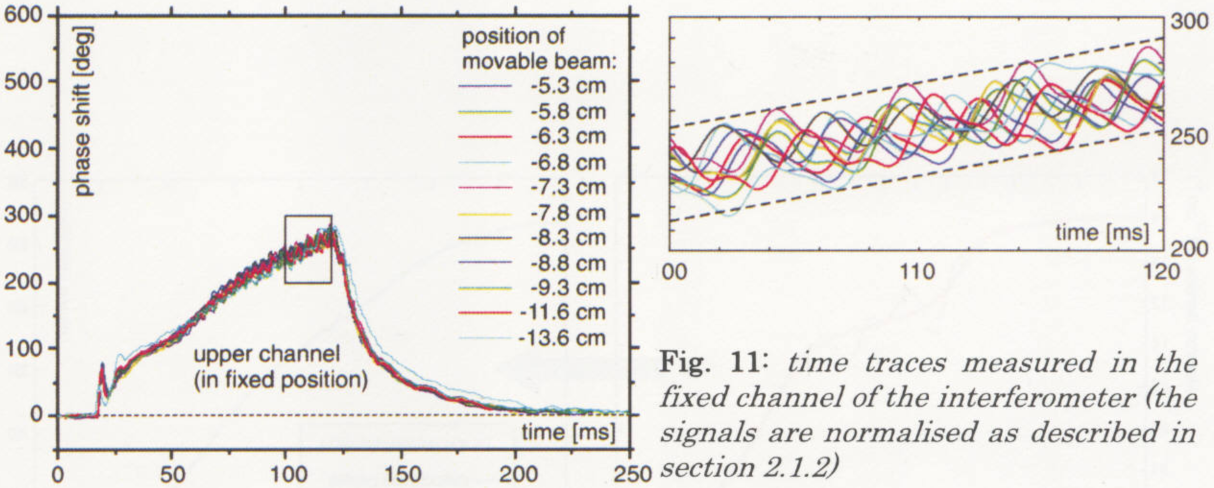

Fig. 11: *time traces measured in the fixed channel of the interferometer (the signals are normalised as described in section 2.1.2)*

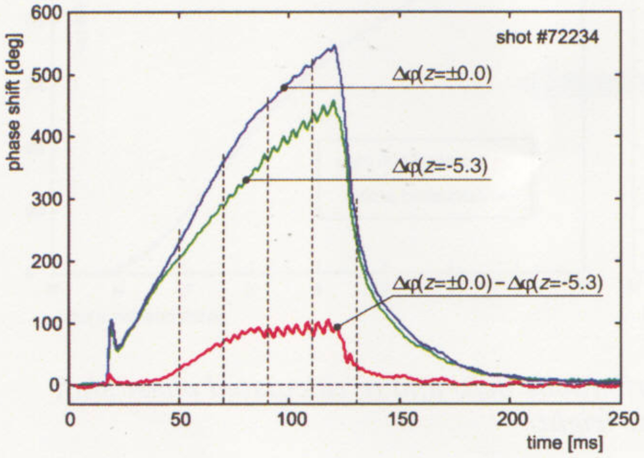

Fig. 12: *phase shift signals ∝ $\int n_e ds$ measured simultaneously in shot #72234 (the vertical lines mark the times for reconstruction of the density distribution; see Fig. 13).*

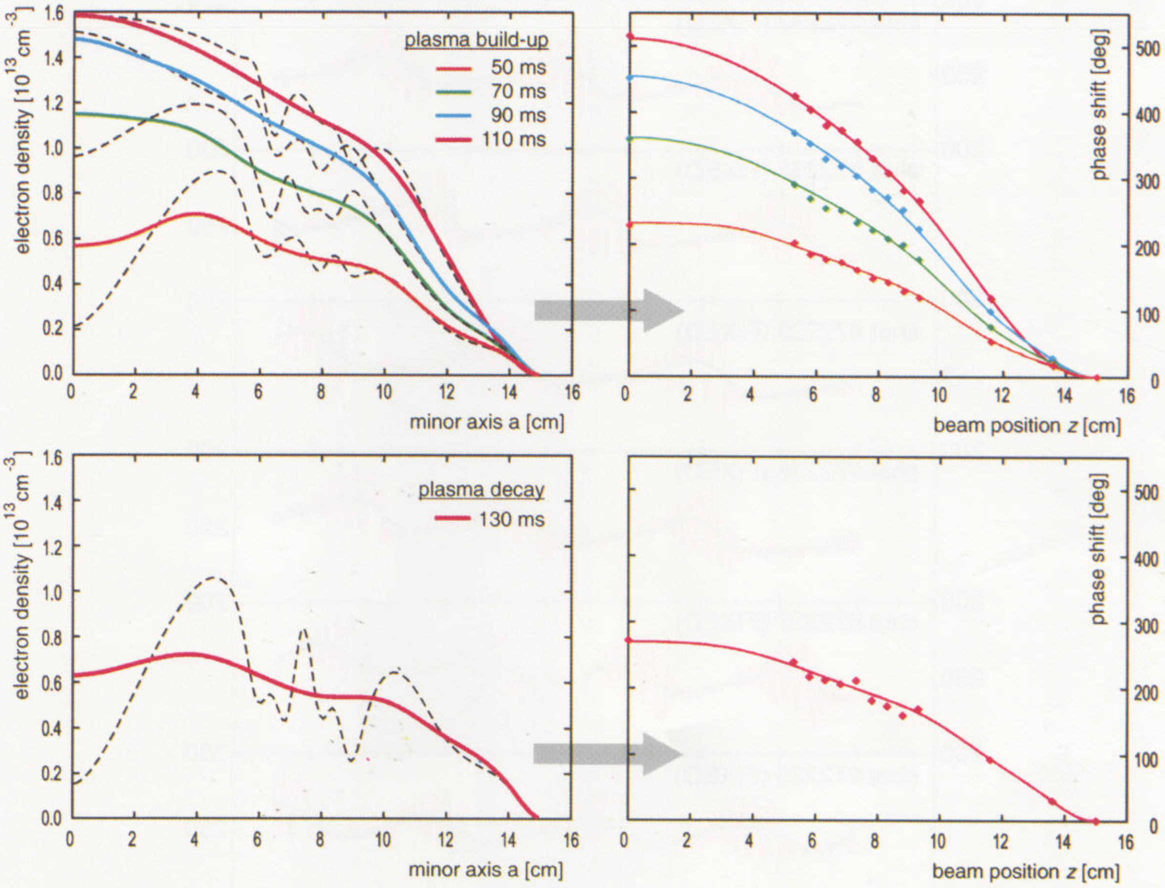

Fig.13: *electron density distributions at different times in the discharge (the dashed lines result from Abel inversion of phase shift profiles, which were constructed by means of spline interpolation; the coloured lines are smooth distributions, for which the re-calculated phase shift profiles conform to the experimental data within reasonable error bars).*

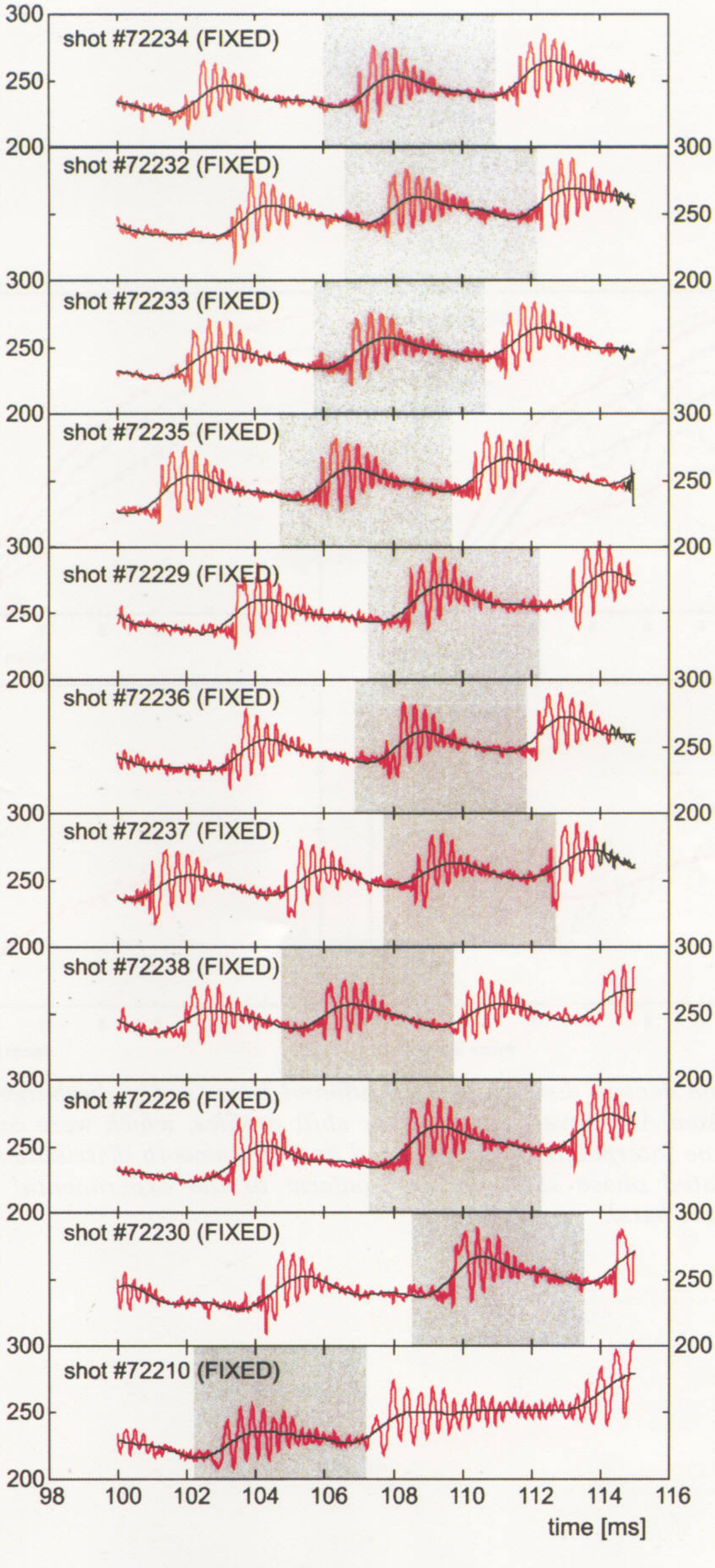

Fig. 14: *interferometric signals measured by the* *fixed* *probing beam in a series of discharges; the shaded regions indicate the selected time intervals (black lines: signals after low-pass filtering).*

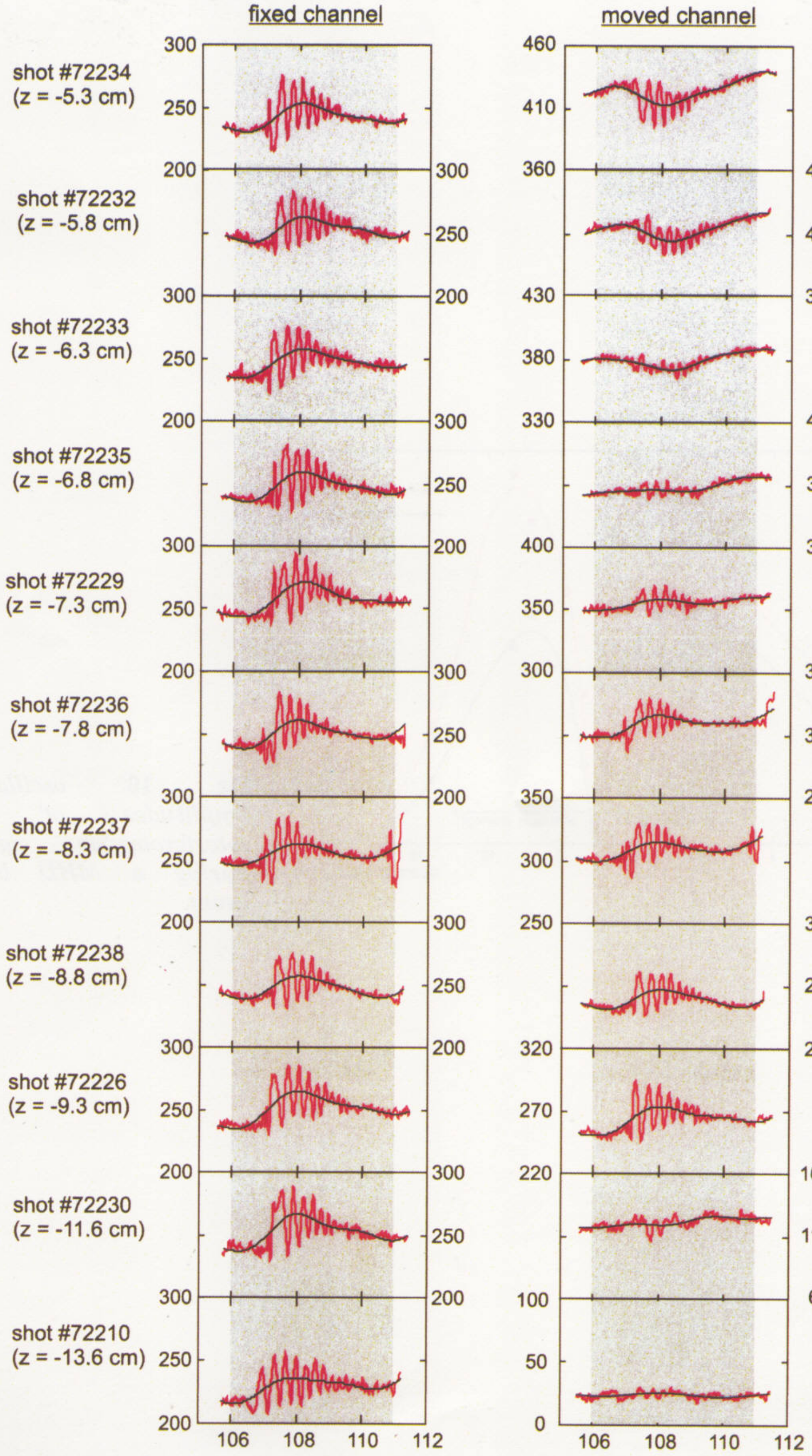

Fig. 15: *interferometric signals of the fixed (left) and the moved (right) probing beam after alignment of the time axes (black lines: signals after low-pass filtering).*

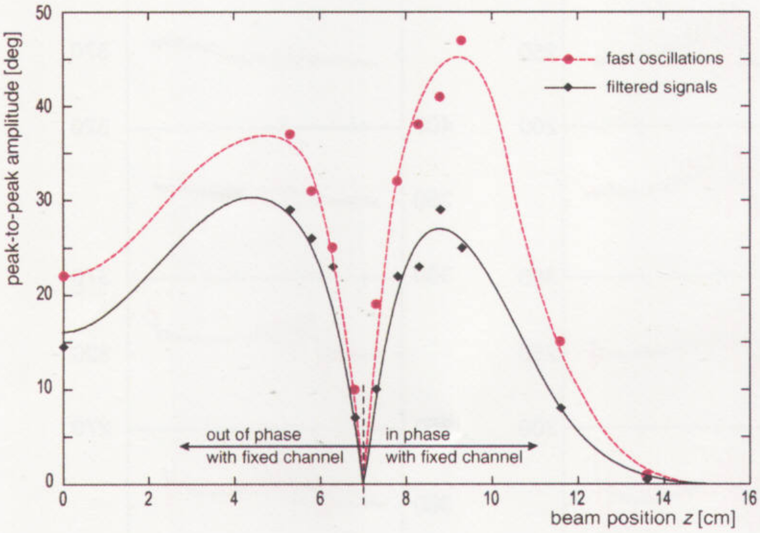

Fig. 16: *oscillation amplitudes of the interferometric signals during a MHD burst event.*

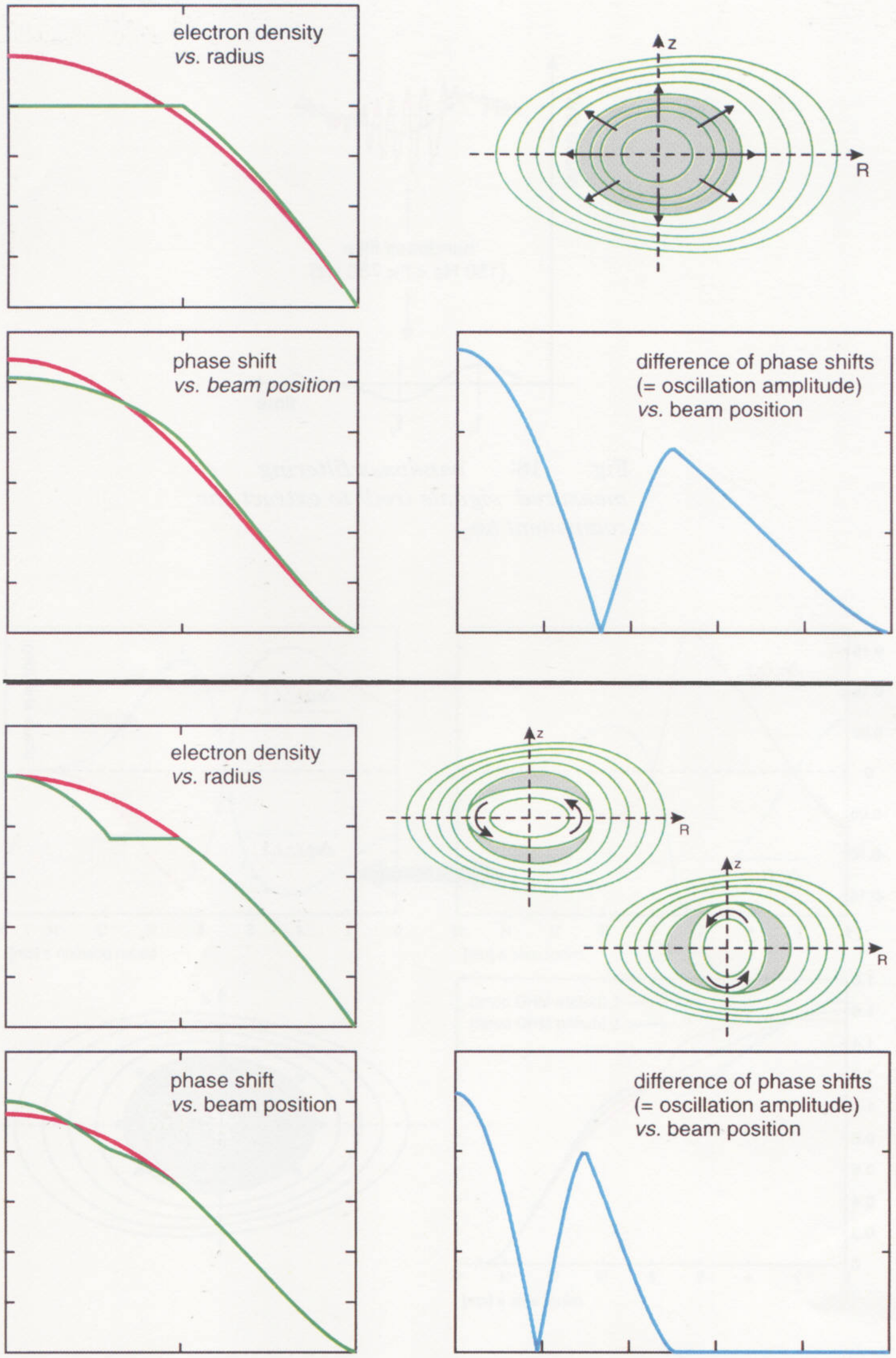

Fig. 17: *schematic representation of a* m=0 *and a* m=2 *perturbation of the density distribution in CHS together with the phase shift profiles and the difference between these profiles for the extreme line-averaged densities in both cases (the latter correspond to the oscillation amplitudes that would be observed under periodic conditions).*

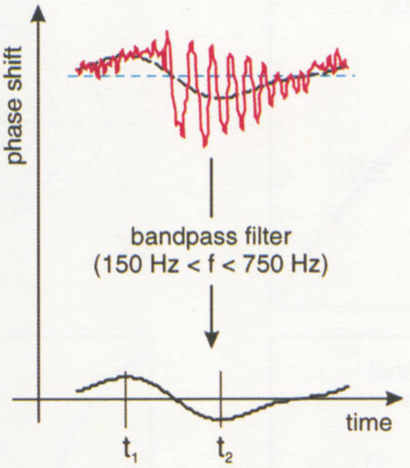

Fig. 18: *bandpass-filtering of measured signals (red) to extract the component* $\Delta\varphi_2$.

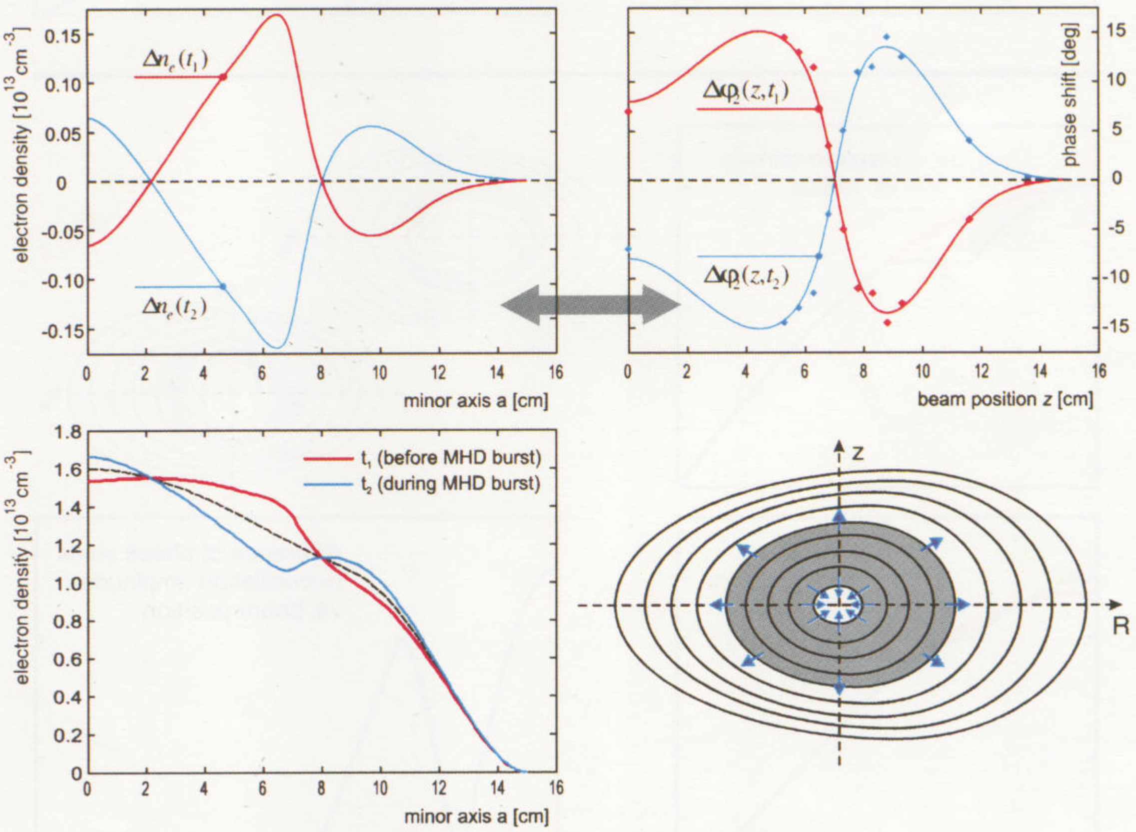

Fig. 19 *(see text for details)*

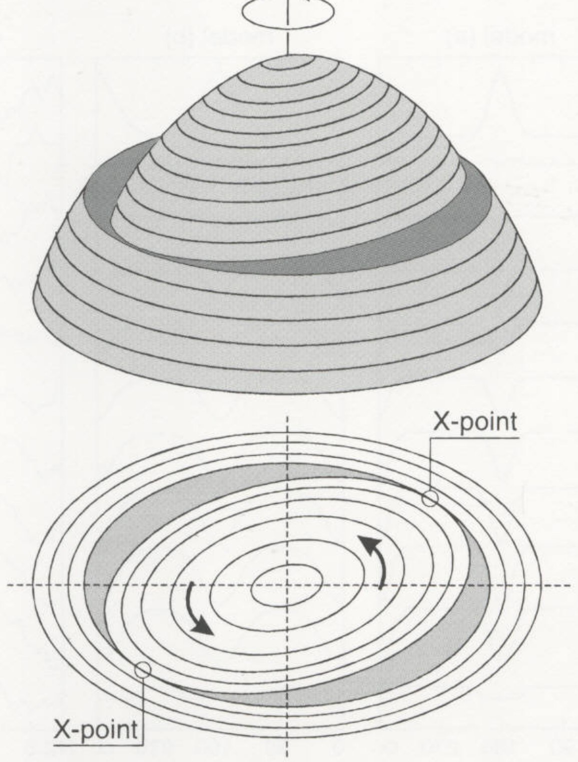

Fig. 20: *three-dimensional view and contour lines of the electron density distribution used for model calculations (rotating plasma core on top of a stationary pedestal).*

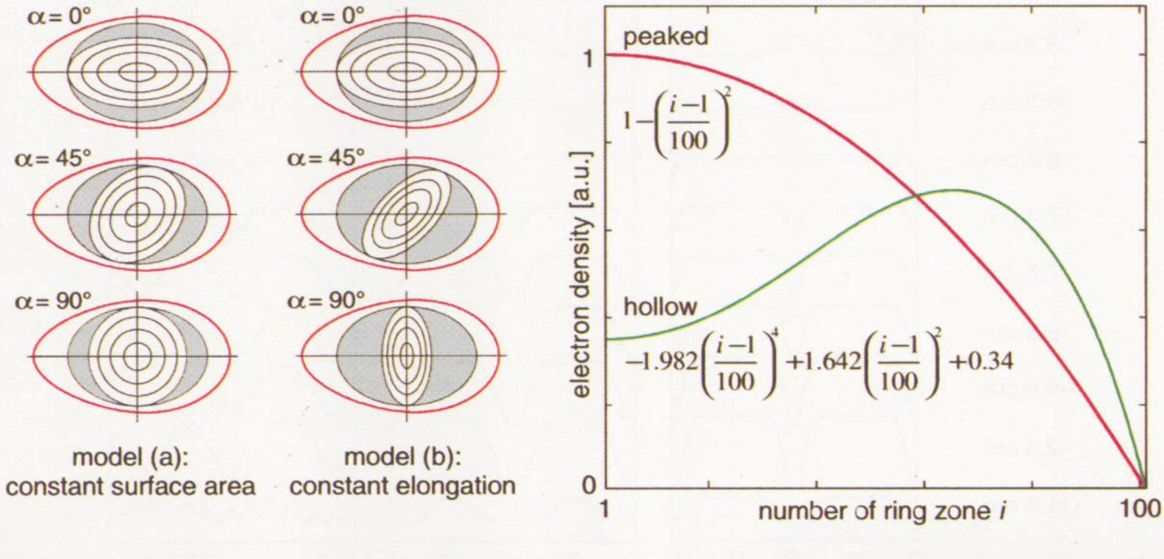

Fig. 21: *__left__: illustration of the rotating plasma core used for model calculations (red circumferences indicate cross-section of CHS); __right__: assumed electron density in the ring zones of the plasma core (distributions are normalised to yield the same total number of electrons).*

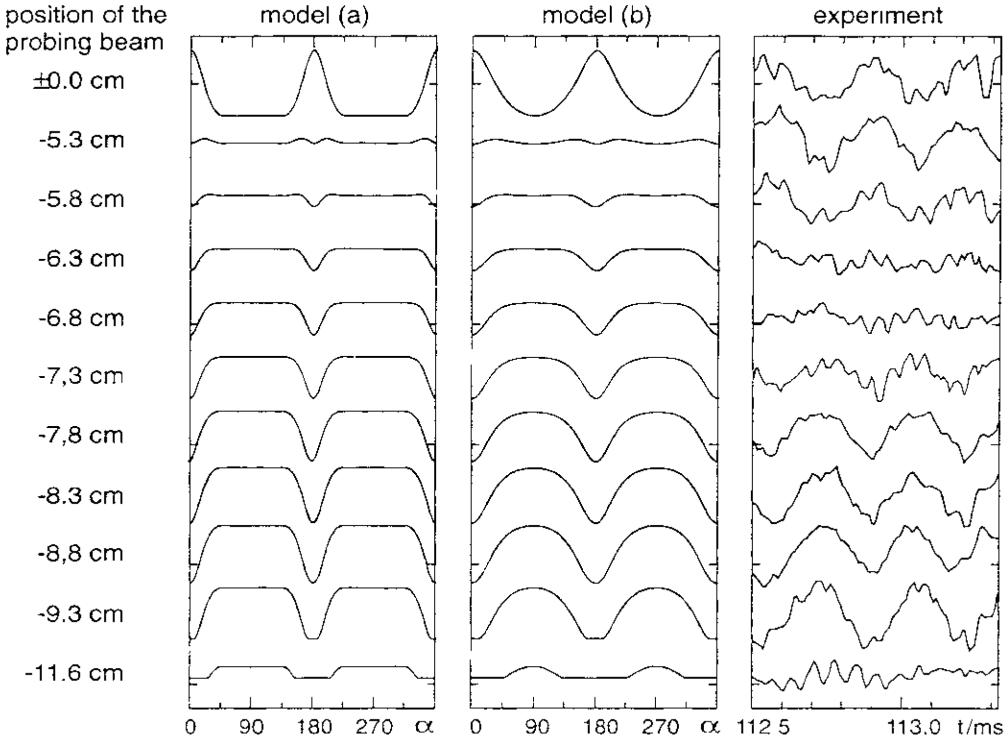

Fig. 22: *simulation of fast signal oscillations assuming a* ***peaked*** *electron density distribution.*

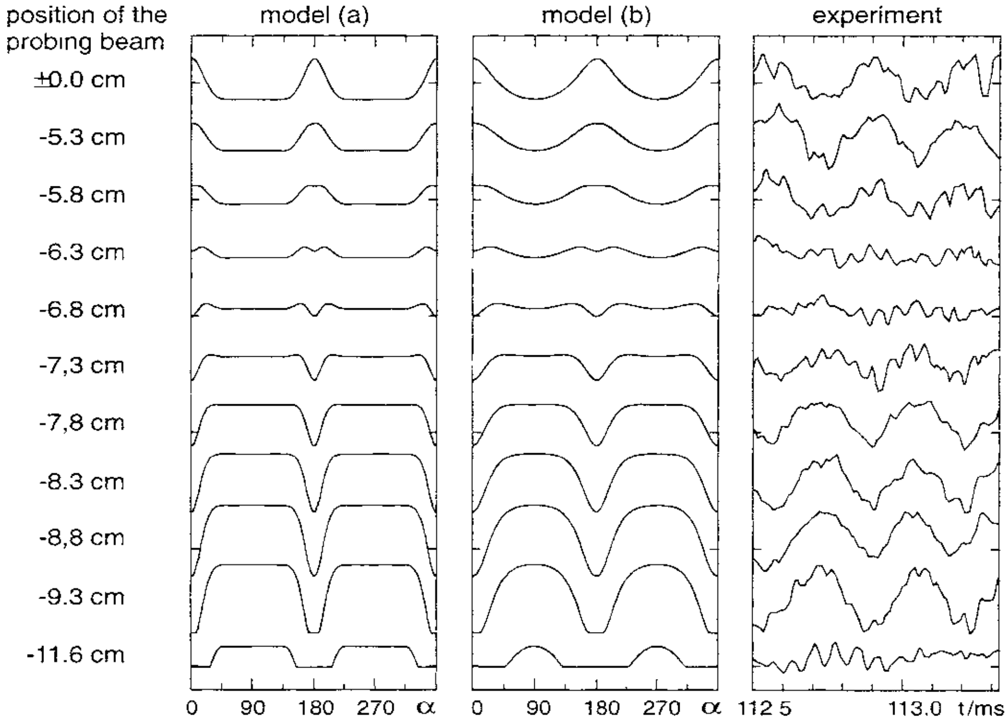

Fig.23: *simulation of fast signal oscillations assuming a* ***hollow*** *electron density distribution.*

Recent Issues of NIFS Series

NIFS-579 M. Tanaka, A Yu Grosberg and T. Tanaka,
Molecular Dynamics of Strongly-Coupled Multichain Coulomb Polymers in Pure and Salt Aqueous Solutions, Nov 1998

NIFS-580 J. Chen, N. Nakajima and M. Okamoto,
Global Mode Analysis of Ideal MHD Modes in a Heliotron/Torsatron System: I. Mercier-unstable Equilibria; Dec. 1998

NIFS-581 M. Tanaka, A Yu Grosberg and T Tanaka,
Comparison of Multichain Coulomb Polymers in Isolated and Periodic Systems: Molecular Dynamics Study; Jan. 1999

NIFS-582 V.S. Chan and S. Murakami,
Self-Consistent Electric Field Effect on Electron Transport of ECH Plasmas; Feb. 1999

NIFS-583 M. Yokoyama, N. Nakajima, M. Okamoto, Y. Nakamura and M. Wakatani,
Roles of Bumpy Field on Collisionless Particle Confinement in Helical-Axis Heliotrons, Feb. 1999

NIFS-584 T.-H. Watanabe, T. Hayashi, T Sato, M. Yamada and H. Ji,
Modeling of Magnetic Island Formation in Magnetic Reconnection Experiment; Feb. 1999

NIFS-585 R. Kumazawa, T Mutoh, T. Seki, F. Shinpo, G. Nomura, T. Ido, T. Watari, Jean-Marie Noterdaeme and Yangping Zhao,
Liquid Stub Tuner for Ion Cyclotron Heating; Mar 1999

NIFS-586 A. Sagara, M. Iima, S. Inagaki, N. Inoue, H. Suzuki, K. Tsuzuki, S. Masuzaki, J. Miyazawa, S. Morita, Y. Nakamura, N. Noda, B. Peterson, S. Sakakibara, T. Shimozuma, H. Yamada, K. Akaishi, H. Chikaraishi, H. Funaba, O. Kaneko, K. Kawahata, A. Komori, N. Ohyabu, O. Motojima, LHD Exp. Group 1, LHD Exp. Group 2,
Wall Conditioning at the Starting Phase of LHD; Mar. 1999

NIFS-587 T. Nakamura and T. Yabe,
Cubic Interpolated Propagation Scheme for Solving the Hyper-Dimensional Vlasov-Poisson Equation in Phase Space; Mar. 1999

NIFS-588 W.X. Wnag, N. Nakajima, S. Murakami and M. Okamoto,
An Accurate δf Method for Neoclassical Transport Calculation ; Mar 1999

NIFS-589 K. Kishida, K. Araki, S. Kishiba and K. Suzuki,
Local or Nonlocal? Orthonormal Divergence-free Wavelet Analysis of Nonlinear Interactions in Turbulence; Mar. 1999

NIFS-590 K. Araki, K. Suzuki, K. Kishida and S. Kishiba,
Multiresolution Approximation of the Vector Fields on T^3, Mar. 1999

NIFS-591 K. Yamazaki, H. Yamada, K.Y Watanabe, K. Nishimura, S. Yamaguchi, H Nakanishi, A. Komori, H Suzuki, T Mito, H. Chikaraishi, K. Murai, O. Motojima and the LHD Group,
Overview of the Large Helical Device (LHD) Control System and Its First Operation; Apr. 1999

NIFS-592 T. Takahashi and Y. Nakao,
Thermonuclear Reactivity of D-T Fusion Plasma with Spin-Polarized Fuel; Apr. 1999

NIFS-593 H. Sugama,
Damping of Toroidal Ion Temperature Gradient Modes; Apr. 1999

NIFS-594 Xiaodong Li,
Analysis of Crowbar Action of High Voltage DC Power Supply in the LHD ICRF System; Apr. 1999

NIFS-595 K. Nishimura, R. Horiuchi and T. Sato,
Drift-kink Instability Induced by Beam Ions in Field-reversed Configurations, Apr. 1999

NIFS-596 Y. Suzuki, T-H. Watanabe, T. Sato and T. Hayashi,
Three-dimensional Simulation Study of Compact Toroid Plasmoid Injection into Magnetized Plasmas; Apr. 1999

NIFS-597 H. Sanuki, K. Itoh, M. Yokoyama, A. Fujisawa, K. Ida, S. Toda, S.-I. Itoh, M. Yagi and A. Fukuyama,
Possibility of Internal Transport Barrier Formation and Electric Field Bifurcation in LHD Plasma;
May 1999

NIFS-598 S. Nakazawa, N. Nakajima, M. Okamoto and N. Ohyabu,
One Dimensional Simulation on Stability of Detached Plasma in a Tokamak Divertor June 1999

NIFS-599 S. Murakami, N. Nakajima, M. Okamoto and J. Nhrenberg,
Effect of Energetic Ion Loss on ICRF Heating Efficiency and Energy Confinement Time in Heliotrons;
June 1999

NIFS-600 R. Horiuchi and T. Sato,
Three-Dimensional Particle Simulation of Plasma Instabilities and Collisionless Reconnection in a Current Sheet;; June 1999

NIFS-601 W. Wang, M. Okamoto, N. Nakajima and S. Murakami,
Collisional Transport in a Plasma with Steep Gradients; June 1999

NIFS-602 T. Mutoh, R. Kumazawa, T. Saki, K. Saito, F. Simpo, G. Nomura, T. Watari, X. Jikang, G. Cattanei, H. Okada, K. Ohkubo, M. Sato, S. Kubo, T. Shimozuma, H. Idei, Y. Yoshimura, O. Kaneko, Y. Takeiri, M. Osakabe, Y. Oka, K. Tsumori, A. Komori, H. Yamada, K. Watanabe, S. Sakakibara, M. Shoji, R. Sakamoto, S. Inagaki, J. Miyazawa, S. Morita, K. Tanaka, B.J. Peterson, S. Murakami, T. Minami, S. Ohdachi, S. Kado, K. Narihara, H. Sasao, H. Suzuki, K. Kawahata, N. Ohyabu, Y. Nakamura, H. Funaba, S. Masuzaki, S. Muto, K. Sato, T. Morisaki, S. Sudo, Y. Nagayama, T. Watanabe, M. Sasao, K. Ida, N. Noda, K. Yamazaki, K. Akaishi, A. Sagara, K. Nishimura, T. Ozaki, K. Toi, O. Motojima, M. Fujiwara, A. Iiyoshi and LHD Exp. Group 1 and 2,
First ICRF Heating Experiment in the Large Helical Device; July 1999

NIFS-603 P.C. de Vries, Y. Nagayama, K. Kawahata, S. Inagaki, H. Sasao and K. Nagasaki,
Polarization of Electron Cyclotron Emission Spectra in LHD; July 1999

NIFS-604 W. Wang, N. Nakajima, M. Okamoto and S. Murakami,
δf Simulation of Ion Neoclassical Transport; July 1999

NIFS-605 T. Hayashi, N. Mizuguchi, T. Sato and the Complexity Simulation Group,
Numerical Simulation of Internal Reconnection Event in Spherical Tokamak; July 1999

NIFS-606 M. Okamoto, N. Nakajima and W. Wang,
On the Two Weighting Scheme for δf Collisional Transport Simulation, Aug. 1999

NIFS-607 O. Motojima, A.A. Shishkin, S. Inagaki, K.Y. Watanabe,
Possible Control Scenario of Radial Electric Field by Loss-Cone-Particle Injection into Helical Device; Aug. 1999

NIFS-608 R. Tanaka, T. Nakamura and T. Yabe,
Constructing Exactly Conservative Scheme in Non-conservative Form; Aug. 1999

NIFS-609 H. Sugama,
Gyrokinetic Field Theory; Aug. 1999

NIFS-610 M. Takechi, G. Matsunaga, S. Takagi, K. Ohkuni, K. Toi, M. Osakabe, M. Isobe, S. Okamura, K. Matsuoka, A. Fujisawa, H. Iguchi, S. Lee, T. Minami, K. Tanaka, Y. Yoshimura and CHS Group, Core Localized Toroidal Alfven Eigenmodes Destabilized By Energetic Ions in the CHS Heliotron/Torsatron,Sep 1999

NIFS-611
K Ichiguchi,
MHD Equilibrium and Stability in Heliotron Plasmas;Sep 1999

NIFS-612
Y Sato, M. Yokoyama, M. Wakatani and V. D Pusovitov,
Complete Suppression of Pfirsch-Schluter Current in a Toroidal l=3 Stellarator,Oct 1999

NIFS-613
S Wang, H. Sanuki and H. Sugama,
Reduced Drift Kinetic Equation for Neoclassical Transport of Helical Plasmas in Ultra-low Collisionality Regime;Oct 1999

NIFS-614
J Miyazawa, H. Yamada, K. Yasui, S Kato, N., Fukumoto, M. Nagata and T Uyama,
Design of Spheromak Injector Using Conical Accelerator for Large Helical Device;Nov. 1999

NIFS-615
M Uchida, A Fukuyama, K Itoh, S.-I Itoh and M Yagi,
Analysis of Current Diffusive Ballooning Mode in Tokamaks; Dec 1999

NIFS-616
M. Tanaka, A.Yu Grosberg and T Tanaka,
Condensation and Swelling Behavior of Randomly Charged Multichain Polymers by Molecular Dynamics Simulations; Dec 1999

NIFS-617
S. Goto and S. Kida,
Sparseness of Nonlinear Coupling; Dec 1999

NIFS-618
M.M. Skoric, T. Sato, A. Maluckov and M S Jovanovic,
Complexity in Laser Plasma Instabilities Dec. 1999

NIFS-619
T -H. Watanabe, H Sugama and T. Sato,
Non-dissipative Kinetic Simulation and Analytical Solution of Three-mode Equations of Ion Temperature Gradient Instability; Dec 1999

NIFS-620
Y Oka, Y. Takeiri, Yu I.Belchenko, M. Hamabe, O Kaneko, K. Tsumori, M. Osakabe, E. Asano, T. Kawamoto, R. Akiyama,
Optimization of Cs Deposition in the 1/3 Scale Hydrogen Negative Ion Source for LHD-NBI System ,Dec 1999

NIFS-621
Yu.I Belchenko, Y Oka, O Kaneko, Y. Takeiri, A. Krivenko, M Osakabe, K Tsumori, E Asano, T Kawamoto, R. Akiyama,
Recovery of Cesium in the Hydrogen Negative Ion Sources;Dec. 1999

NIFS-622
Y Oka, O. Kaneko, K. Tsumori, Y. Takeiri, M Osakabe, T Kawamoto, E. Asano, and R. Akiyama,
H- Ion Source Using a Localized Virtual Magnetic Filter in the Plasma Electrode: Type I LV Magnetic Filter: Dec 1999

NIFS-623
M. Tanaka, S Kida, S. Yanase and G. Kawahara,
Zero-absolute-vorticity State in a Rotating Turbulent Shear Flow;Jan 2000

NIFS-624
F Leuterer, S. Kubo,
Electron Cyclotron Current Drive at $\omega \approx \omega_c$ with X-mode Launched from the Low Field Side; Feb 2000

NIFS-625
K Nishimura,
Wakefield of a Charged Particulate Influenced by Emission Process of Secondary Electrons; Mar 2000

NIFS-626
K Itoh, M Yagi, S-I Itoh, A Fukuyama,
On Turbulent Transport in Burning Plasmas;

Mar. 2000

NIFS-627 K. Itoh, S.-I. Itoh, L. Giannone,
Modelling of Density Limit Phenomena in Toroidal Helical Plasmas; Mar. 2000

NIFS-628 K. Akaishi, M. Nakasuga and Y. Funato,
True and Measured Outgassing Rates of a Vacuum Chamber with a Reversibly Absorbed Phase; Mar. 2000

NIFS-629 T. Yamagishi,
Effect of Weak Dissipation on a Drift Orbit Mapping; Mar. 2000

NIFS-630 S. Toda, S.-I, Itoh, M. Yagi, A. Fukuyama and K. Itoh,
Spatial Structure of Compound Dither in L/H Transition; Mar 2000

NIFS-631 N. Ishihara and S. Kida,
Axial and Equatorial Magnetic Dipoles Generated in a Rotating Spherical Shell; Mar. 2000

NIFS-632 T. Kuroda, H. Sugama, R. Kanno and M. Okamoto,
Ion Temperature Gradient Modes in Toroidal Helical Systems; Apr. 2000

NIFS-633 V.D. Pustovitov,
Magnetic Diagnostics: General Principles and the Problem of Reconstruction of Plasma Current and Pressure Profiles in Toroidal Systems; Apr 2000

NIFS-634 A.B. Mikhailovskii, S.V. Konovalov, V.D Pustovitov and V.S. Tsypin,
Mechanism of Viscosity Effect on Magnetic Island Rotation; Apr. 2000

NIFS-635 H. Naitou, T. Kuramoto, T. Kobayashi, M. Yagi, S. Tokuda and T. Matsumoto,
Stabilization of Kinetic Internal Kink Mode by Ion Diamagnetic Effects; Apr. 2000

NIFS-636 A. Kageyama and S. Kida,
A Spectral Method in Spherical Coordinates with Coordinate Singularity at the Origin; Apr. 2000

NIFS-637 R. Horiuchi, W. Pei and T. Sato,
Collisionless Driven Reconnection in an Open System; June 2000

NIFS-638 K. Nagaoka, A. Okamoto, S. Yoshimura and M.Y. Tanaka,
Plasma Flow Measurement Using Directional Langmuir Probe under Weakly Ion-Magnetized Conditions; July 2000

NIFS-639 Alexei Ivanov,
Scaling of the Distribution Function and the Critical Exponents near the Point of a Marginal Stability under the Vlasov-Poisson Equations; Aug. 2000

NIFS-640 K. Ohi, H. Naitou, Y. Tauchi, O. Fukumasa,
Observation of the Limit Cycle in the Asymmetric Plasma Divided by the Magnetic Filter; Aug. 2000

NIFS-641 H. Momota, G.H. Miley and J. Nadler,
Direct Energy Conversion for IEC Propulsions; Aug. 2000

NIFS-642 Y. Kondoh, T. Takahashi and H. Momota,
Revisit to the Helicity and the Generalized Self-organization Theory; Sep. 2000

NIFS-643 H. Soltwisch, K. Tanaka,
Changes of the Electron Density Distribution during MHD Activity in CHS Sep. 2000